

EFFECT OF AMBIPOLAR DIFFUSION ON THE NON-LINEAR EVOLUTION OF MAGNETOROTATIONAL INSTABILITY IN WEAKLY IONIZED DISKS

XUE-NING BAI & JAMES M. STONE

Department of Astrophysical Sciences, Princeton University, Princeton, NJ, 08544

Draft version June 3, 2018

ABSTRACT

We study the role of ambipolar diffusion (AD) on the non-linear evolution of the MRI in protoplanetary disks using the strong coupling limit, which applies when the electron recombination time is much shorter than the orbital time. The effect of AD in this limit is characterized by the dimensionless number Am , the frequency of which neutral particles collide with ions normalized to the orbital frequency. We perform three-dimensional unstratified shearing-box simulations of the MRI over a wide range of Am as well as different magnetic field strengths and geometries. The saturation level of the MRI turbulence depends on the magnetic geometry and increases with the net magnetic flux. There is an upper limit to the net flux for sustained turbulence, corresponding to the requirement that the most unstable vertical wavelength be less than the disk scale height. Correspondingly, at a given Am , there exists a maximum value of the turbulent stress α_{\max} . For $Am \lesssim 1$, the largest stress is associated with a field geometry that has both net vertical and toroidal flux. In this case, we confirm the results of linear analyses that show the fastest growing mode has a non-zero radial wave number with growth rate exceeding the pure vertical field case. We find there is a very tight correlation between the turbulent stress α and the plasma $\langle\beta\rangle \equiv P_{\text{gas}}/P_{\text{mag}} \approx 1/2\alpha$ at the saturated state of the MRI turbulence regardless of field geometry, and α_{\max} rapidly decreases with decreasing Am . In particular, we find $\alpha_{\max} \approx 7 \times 10^{-3}$ for $Am = 1$ and $\alpha_{\max} \approx 6 \times 10^{-4}$ for $Am = 0.1$.

Subject headings: magnetohydrodynamics — instabilities — methods: numerical — planetary systems: protoplanetary disks — turbulence

1. INTRODUCTION

One of the most fundamental questions in accretion disk dynamics is how the disk transports angular momentum and accretes to the central object. The magnetorotational instability (MRI, Balbus & Hawley 1991) is widely considered to be the most likely mechanism for the transport process. The non-linear evolution of the MRI under ideal MHD conditions has been studied extensively using both local (Hawley et al. 1995; Stone et al. 1996; Miller & Stone 2000) and global (Armitage 1998; Hawley 2000, 2001; Fromang & Nelson 2006) numerical simulations. It has been found that MRI generates vigorous MHD turbulence and produce efficient outward transport of angular momentum whose rate is compatible with observations. However, accretion disks in some systems are only partially ionized, and non-ideal MHD effects need to be taken into account. In particular, most regions of the protoplanetary disks (PPDs) are too cold for sufficient thermal ionization, and effective ionization may be achieved only in the disk surface layer due to external ionization sources such as X-ray radiation from the central star and cosmic ray ionization (Gammie 1996; Stone et al. 2000). Non-ideal MHD effects reflect the incomplete coupling between the disk material and the magnetic field, and substantially affect the growth and saturation of the MRI.

There are three non-ideal MHD effects as manifested in the generalized Ohm's law, namely the Ohmic resistivity, Hall effect and ambipolar diffusion (AD), with three different regimes associated with the relative importance

of these terms. In general, the Ohmic term dominates at high density and very low ionization, the AD term dominates in the opposite limit, and the Hall term is important in between. So far the majority of studies have been focused on the Ohmic regime. In this case, MRI is damped when the Elsasser number $\Lambda \equiv v_{\text{Az}}^2/\eta\Omega$ falls below order unity (Jin 1996; Turner et al. 2007), where v_{Az} is the Alfvén velocity in the vertical direction, η is the Ohmic resistivity, Ω is the angular frequency of Keplerian rotation. Another often quoted criterion is the magnetic Reynolds number $\text{Re}_M \equiv c_s^2/\eta\Omega \gtrsim 10^4$ for MRI to be self-sustained (where c_s is the sound speed), which has the advantage of being independent of the magnetic field (Fleming et al. 2000). Ohmic resistivity has been used extensively to model the layered accretion in PPDs, where the surface layer of the disk is sufficiently ionized to couple to the magnetic field and drive the MRI turbulence, while the midplane region is too poorly ionized and “dead” (Fleming & Stone 2003; Turner et al. 2007; Turner & Sano 2008; Ilgner & Nelson 2008; Oishi & Mac Low 2009).

The importance of Hall and AD terms in PPDs has been studied in a number of theoretical works, but relatively little attention has been paid to numerical simulations of the non-linear regime. Linear analysis of the MRI in the Hall regime have been performed by Wardle (1999) and Balbus & Terquem (2001). The growth rate is strongly affected by the Hall term and depends on the sign of $\mathbf{B} \cdot \boldsymbol{\Omega}$. Nevertheless, numerical simulations including both the Hall and Ohmic terms (where the Ohmic term dominates) showed that the Hall term does not strongly affect the saturation amplitude of MRI

(Sano & Stone 2002a,b). It is yet to study the behavior of MRI in the regime where Hall effect dominates over other terms, and to include the Hall term in the more realistic vertically stratified simulations.

The relative motion between ions and neutrals leads to AD. AD is ideally studied using the two-fluid approach, where the ions and neutrals are treated as separate fluids, coupled by the ion-neutral drag via collisions. Moreover, ion and neutral densities are affected by the ionization and recombination processes. Most analytical studies in the linear regime adopt the Boussinesq approximation where ion and neutral densities are kept constant (Blaes & Balbus 1994; Kunz & Balbus 2004; Desch 2004). These studies show that the growth of MRI is suppressed when the collision frequency of a neutral with the ions falls below the orbital frequency. In the mean time, when both vertical and azimuthal field is present, unstable modes always exist due to the effect of AD, and these unstable modes require non-zero radial wavenumbers (Kunz & Balbus 2004; Desch 2004). Blaes & Balbus (1994) also studied the effect of ionization and recombination with compressibility (for vertical propagating waves), and found that the presence of azimuthal and radial field allows the coupling to acoustic and ionization modes, and the azimuthal field tends to stabilize the flow when the recombination time is not too long compared with dynamical time.

The effect AD on the MRI in the non-linear regime was first studied by Mac Low et al. (1995). They implemented and tested AD in the “strong coupling” limit (see below) in the ZEUS code and performed simulations with net vertical flux for various ion-neutral coupling strengths. Their results confirmed the stability analysis of Blaes & Balbus (1994), but their simulations are only two-dimensional and did not follow the evolution much beyond the linear stage. In another study, Brandenburg et al. (1995) included the effect of AD (also in the strong coupling limit) in their three-dimensional simulations of a local, vertically stratified disk. They found that turbulence remains self-sustained in a case where AD time is long compared with orbital time, although reduced in strength, and in another case where the AD time was set comparable to Ω^{-1} , turbulence decayed.

A systematic study on the non-linear evolution of MRI with AD is done by Hawley & Stone (1998) (hereafter HS) using three-dimensional (3D) numerical simulations. They used the two-fluid approach without considering the ionization-recombination processes, therefore ions and neutrals obey their own continuity equations. Both net-vertical and net-toroidal magnetic configurations were considered. They found that the system behaves like fully-ionized gas when the ion-neutral collision frequency is greater than 100Ω , while ions and neutrals behave independently when the collision frequency fall below 0.01Ω . The amplitude of magnetic field at saturation is proportional to the ion density when it is much smaller than the neutral density. The two-fluid approach adopted by HS is valid when the recombination time scale is long compared with the dynamical time. However, AD in PPDs is in general in the “strong coupling” limit (Shu 1991). Two conditions must be satisfied in this limit: 1. The ion density ρ_i is negligible compared with the neu-

tral density ρ_n . 2. The electron recombination time τ_r must be much smaller than the orbital frequency Ω . In this limit, the ion density is purely determined by the ionization-recombination equilibrium with the neutrals, and the two-fluid formulation is simplified into a single-fluid formalism (for the neutrals). In PPDs, condition 1 is always satisfied, and we will show in a companion paper (Bai 2011) that condition 2 is almost always satisfied.

In this paper, we conduct three-dimensional (3D) local shearing-box simulations to explore the effect of AD on the non-linear evolution of MRI in the strong coupling limit. This is conceptually different from the simulations performed by HS in that the ion density does not obey continuity equation, and is set by the neutral density due to chemical equilibrium. Effectively, this allows the coupling of the MRI with acoustic and ionization modes, which leads to more complicated interactions (Blaes & Balbus 1994). Moreover, our simulations correspond to the limit where the ion density is negligibly small (i.e., $f \rightarrow 0$ in HS), which is difficult for two-fluid simulations due to the stiffness of the equations. In the strong coupling limit, there is only one controlling parameter, namely, the ion-neutral collision frequency $\gamma\rho_i$. We perform three sets of simulations with net vertical flux, net toroidal flux and both. In each group of runs, we systematically vary $\gamma\rho_i$ as well as the strength of the net field. Our main goal is to study the conditions under which MRI turbulence can be self-sustained or is suppressed due to AD. In addition, we study the properties of the MRI turbulence in the AD dominated regime.

This paper is structured as follows. In Section 2 we provide the formulation of AD in the strong coupling limit, describe the numerical method and code test problems. A series of numerical simulations on the non-linear evolution of MRI with AD are presented and analyzed in Section 3, from which we discuss the condition under which MRI turbulence is sustained or suppressed as well as the properties of the MRI turbulence in AD dominated regime. We conclude and briefly discuss various implications in Section 5.

2. FORMULATION AND NUMERICAL METHOD

2.1. Ambipolar Diffusion in Weakly Ionized Plasma

In weakly ionized plasma, the inertia of the ionized species is negligible. The gas dynamics can thus be described by single-fluid equations for the neutrals, modified by non-ideal MHD effects. The effect of ambipolar diffusion (AD) derives from the relative motion between the ions and the neutrals. Since the ion inertia is negligible, the ion velocity is determined by the balance between the Lorentz force and the ion-neutral collisional drag

$$\frac{\mathbf{J} \times \mathbf{B}}{n_i} = \gamma \rho m_i (\mathbf{v}_i - \mathbf{v}), \quad (1)$$

where m_i , n_i and \mathbf{v}_i are the ion mass, number density and velocity respectively, ρ , \mathbf{v} are the density and velocity of the neutrals, \mathbf{J} , \mathbf{B} are the current density and magnetic field vectors, $\gamma = \langle \sigma v \rangle / (m_n + m_i)$, with $\langle \sigma v \rangle$ begin the rate coefficient for momentum transfer between the ions and the neutrals and m_n the neutral mass. The magnetic field is effectively carried by the ions, thus the induction

equation now reads

$$\begin{aligned} \frac{\partial \mathbf{B}}{\partial t} &= \nabla \times (\mathbf{v} \times \mathbf{B}) + \nabla \times \left[\frac{(\mathbf{J} \times \mathbf{B}) \times \mathbf{B}}{c\gamma\rho\rho_i} \right] \\ &= \nabla \times (\mathbf{v} \times \mathbf{B}) - \frac{4\pi}{c} \nabla \times \left(\frac{v_A^2}{\gamma\rho_i} \mathbf{J}_\perp \right), \end{aligned} \quad (2)$$

where ρ_i is the ion mass density, $v_A \equiv B/\sqrt{4\pi\rho}$ is the Alfvén velocity, \mathbf{J}_\perp is the component of the current density that is perpendicular to the direction of the magnetic field. The second term on the right hand side is the AD term, from which the ambipolar diffusivity can be defined as $\eta_A = v_A^2/\gamma\rho_i$. The rest of the fluid equations remain the same as the ideal MHD equations. In particular, the momentum equation is unchanged since the neutrals effectively feel the magnetic tension and pressure by the ion-neutral collisions.

The above derivation is strictly valid when electrons and ions are the only charge carriers, and all ions have the same mass. Nevertheless, the effect of multiple ion and charged grain species can be combined into an effective AD coefficient¹. AD becomes the dominant non-ideal MHD effect when the gyro-frequency of both the ions and the electrons are higher than their collision frequency with the neutrals (i.e., both ions and electrons are coupled to the magnetic field). In practice, this corresponds to regions with low density and strong magnetic field.

The effect of AD in rotating disks (with angular frequency Ω) is characterized by the parameter Am (Chiang & Murray-Clay 2007):

$$Am \equiv \frac{\gamma\rho_i}{\Omega}, \quad (3)$$

which is the number of effective collisions for a neutral molecule/atom with the ions in a dynamical time $1/\Omega$. Physically, we see that $Am = v_A^2/\eta_A\Omega$, which is equivalent to the Elsasser number for Ohmic resistivity $\Lambda = v_A^2/\eta\Omega$. Therefore, Am measures the ratio of the AD time scale over the critical wavelength v_A/Ω and the dynamical time scale.

In this paper, we study AD in the strong coupling limit (Shu 1991): the electron (ion) recombination time is much shorter than the dynamical time $1/\Omega$ so that the ion density ρ_i is determined by the local thermodynamical quantities (density and temperature). The strong coupling limit is widely applicable in protoplanetary disks, and we show in our companion paper (Bai 2011) that the recombination time is typically at least one order of magnitude smaller than the dynamical time, even in the disk coronal regions. Using the strong coupling limit, we assume the ion density depends on the neutral density ρ in the form of

$$\rho_i = \rho_{i0} \left(\frac{\rho}{\rho_0} \right)^\nu, \quad (4)$$

where ρ_{i0} and ρ_0 are the reference density of the ions and the neutrals. A simple-minded calculation of the

ionization-recombination equilibrium gives $\xi\rho = C\rho_i^2$, which yields $\nu = 1/2$. In the equation ξ is the ionization rate, of the order 10^{-17} s^{-1} , C is the effective rate coefficient for recombination, of the order $10^{14} \text{ cm}^3 \text{ s}^{-1} \text{ g}^{-1}$ in the absence of grains (Blaes & Balbus 1994). In reality, the recombination process is complicated by a complex network of gas phase and grain phase chemical reactions, and we can address the complications by exploring different values of ν . Being a two-body process in general, and one expects $0 < \nu < 1$.² In fact, our simulations show that the properties of the MRI turbulence is insensitive to ν (see Section 3.1.3).

2.2. Numerical Method

We use Athena, a higher-order Godunov MHD code with constrained transport technique to enforce the divergence-free constraint on the magnetic field (Gardiner & Stone 2005, 2008; Stone et al. 2008) for all calculations presented in this paper. Non-ideal MHD terms including Ohmic resistivity (Davis et al. 2010), the Hall term (in progress) and AD (this paper) have been developed for Athena. We consider a local patch of a Keplerian disk using the standard shearing-box formalism (Goldreich & Lynden-Bell 1965), which adopts a local reference frame at a fiducial radius corotating with the disk at orbital frequency Ω . In this frame, we write the MHD equations with AD in a Cartesian coordinate system as

$$\frac{\partial \rho}{\partial t} + \nabla \cdot (\rho \mathbf{v}) = 0, \quad (5)$$

$$\frac{\partial \rho \mathbf{v}}{\partial t} + \nabla \cdot (\rho \mathbf{v}^T \mathbf{v} + \mathbf{T}) = \rho \left[2\mathbf{v} \times \boldsymbol{\Omega} + 3\Omega^2 x \hat{\mathbf{x}} \right], \quad (6)$$

$$\frac{\partial \mathbf{B}}{\partial t} = \nabla \times \left[\mathbf{v} \times \mathbf{B} + \frac{(\mathbf{J} \times \mathbf{B}) \times \mathbf{B}}{c\gamma_i\rho_i\rho} \right], \quad (7)$$

where \mathbf{T} is the total stress tensor

$$\mathbf{T} = (P + B^2/8\pi) \mathbf{I} - \frac{\mathbf{B}^T \mathbf{B}}{4\pi}, \quad (8)$$

\mathbf{I} is the identity tensor, P is the gas pressure. $\hat{\mathbf{x}}, \hat{\mathbf{y}}, \hat{\mathbf{z}}$ are unit vectors pointing to the radial, azimuthal and vertical directions respectively, where $\boldsymbol{\Omega}$ is along the $\hat{\mathbf{z}}$ direction. Disk vertical gravity is ignored and our simulations are vertically unstratified. We use an isothermal equation of state $P = \rho c_s^2$, where c_s is the isothermal sound speed. Periodic boundary conditions are used in the azimuthal and vertical directions, while the radial boundary conditions are shearing periodic as usual.

An orbital advection scheme (Masset 2000; Johnson et al. 2008) has been implemented in Athena (Stone & Gardiner 2010). It splits the dynamical equations into two systems, one of which corresponds to linear advection operator with background flow velocity $3\Omega x/2\hat{\mathbf{y}}$ and the other evolves only velocity fluctuations. The orbital advection scheme not only accelerates the calculation in large box size by admitting larger time steps, but also makes the calculation more accurate.

¹ A more generalized derivation of all non-ideal MHD terms in the induction equation is given and discussed in Bai (2011) (and see also Wardle (1999, 2007)), which also includes Ohmic resistivity and the Hall term.

² For example, Figure 1a and Figure 3 of Bai & Goodman (2009) illustrate the dependence of electron abundance $x_e \propto \rho_i$ on the gas density in various chemistry models with and without dust grains, and $0 < \nu < 1$ holds in essentially all circumstances.

The last term on the right hand side of equation (7) represents the AD term, where ρ_i is the effective ion density, approximated by equation (4). Non-ideal MHD terms (e.g., the AD term) are implemented in Athena in an operator-split way. Over one time step, one first solves the induction equation using only the non-ideal MHD terms, and then solves ideal MHD equations. The induction equation with AD term is a diffusion equation and is evolved by a fully explicit forward-Euler method. The divergence free condition is maintained using constrained transport: we calculate the AD electromotive force defined at cell edges by interpolating the magnetic field and current density to such locations. The method is stable, with time step constrained to be proportional to grid size squared. The overall method is first order accurate in time.

Numerical method including the AD term has been frequently implemented in the framework of two-fluid models (e.g., Toth 1994; Stone 1997; Smith & Mac Low 1997; Falle 2003; Li et al. 2006; O’Sullivan & Downes 2006, 2007; Tilley & Balsara 2008), with the main applications on star formation, turbulence and shocks in the interstellar medium. However, single-fluid models for AD in the strong coupling limit relevant to weakly ionized disks (Brandenburg et al. 1995; Mac Low et al. 1995) are relatively less studied numerically. Recently, Choi et al. (2009) described an explicit scheme for incorporating AD in the strong coupling limit in an MHD code that is second order accurate, and use super time-stepping to accelerate the calculation when the AD coefficient is large. As we find MRI is suppressed at moderately large AD coefficients (see Section 3), super time-stepping is not needed for the purpose of this paper.

2.3. Code Tests

In this subsection, we conduct two test problems to examine the performance of our implementation of the AD term. For all these tests, we consider non-rotating system and turn off the shearing box source terms on the right hand side of equation (6).

2.3.1. Isothermal C-type Shock Test

The effect of ambipolar diffusion is best manifested in C-type shocks (Draine 1980), which is a shock with continuous transitions consequent of the AD. For the purpose of the code test, here we consider the isothermal C-type test by Mac Low et al. (1995), which has become a standard test problem for AD.

We consider steady-state ($\partial/\partial t = 0$) shock and work in the shock frame, with upstream gas density ρ_0 moving at velocity v_s . The upstream gas is threaded by a uniform magnetic field \mathbf{B}_0 that lies at an angle θ to the velocity. Let \mathbf{v}_s be in the \hat{x} direction, and \mathbf{B}_0 be in the $\hat{x}-\hat{y}$ plane. For a continuous shock, the jump conditions reduce to $\partial/\partial x = 0$. Assuming the ion density ρ_i is constant ($\nu = 0$), the equations that describe the C-type shock read

$$\rho v_x = \rho_0 v_s, \quad (9)$$

$$\rho(v_x^2 + c_s^2) + \frac{B_y^2}{8\pi} = \rho_0(v_s^2 + c_s^2) + \frac{B_{0y}^2}{8\pi}, \quad (10)$$

$$\rho v_x v_y - \frac{B_x B_y}{4\pi} = -\frac{B_x B_{0y}}{4\pi}, \quad (11)$$

$$v_x B_y - v_y B_x - \frac{B^2}{4\pi\rho\gamma\rho_i} \frac{dB_y}{dx} = v_s B_{0y}. \quad (12)$$

Note that $B_x = B_{0x}$ is constant.

The shock is characterized by three dimensionless parameters: the sonic Mach number $M = v_s/c_s$, the Alfvén Mach number $A = v_s/v_A$ (where $v_A^2 = B_0^2/4\pi\rho_0$), and the angle θ of the magnetic field with the upstream flow. The characteristic length scale of the problem is given by $L = v_A/\gamma\rho_i$. We further define $D \equiv \rho/\rho_0$, and $b \equiv B_y/B_0$. After some algebra, we arrive at a dimensionless first order differential equation for D (Mac Low et al. 1995)

$$\left(\frac{1}{D^2} - \frac{1}{M^2}\right) \frac{dD}{d(x/L)} = (b^2 + \cos^2 \theta)^{-1} \times \frac{b}{A} \left[b - D \left(\frac{b - \sin \theta}{A^2} \cos^2 \theta + \sin \theta \right) \right]. \quad (13)$$

One can numerically integrate this ordinary differential equation to obtain the C-type shock profile. In Figure 1 we show a semi-analytical solution for $M = 50$, $A = 10$ and $\theta = \pi/4$ obtained by using a 4th order Runge-Kutta method.

To use this solution as a code test, the shock is set to be aligned with the grid in the \hat{x} direction. We use outflow boundary conditions in this direction. In multi-dimensional tests, periodic boundary conditions are used in other directions. The shock solution should be stationary (i.e., a standing shock), thus we evolve the solution for sufficiently long time ($\sim 5L/c_s$) and compare to the initial conditions. In Figure 1, we further show the absolute error of the shock profile compared with the semi-analytic solution. Since the shock is grid-aligned, 1D, 2D and 3D tests essentially produce the same result. In our tests, the grid resolution is chosen to be 2 and 4 cells per L .³ We see that our code very accurately resolves the structure of the C-type shock using only a few cells per L . The main source of the error lie in the region where density and velocity profile vary quickly. In our comparison, the position of the shock is fixed at the initial place, while in reality, the shock position can shift slightly during numerical relaxation.

2.3.2. Damping of MHD Waves

Linear MHD waves are damped due to AD. Because the exact eigenvectors in the AD regime can be very complicated, we initialize the problem with ideal MHD wave eigenvectors and measure the damping rate. This means the initial conditions are a linear superposition of more than one eigen-mode, but the averaged damping rate should approach the analytical value for a single mode as long as the AD coefficient is sufficiently small.

The analytical damping rate for various MHD waves due to AD can be found in and/or derived from Balsara (1996), as we summarize below. The damping rate of the Alfvén wave is given by the solution of

$$\omega^2 = k^2 v_A^2 \cos^2 \theta \left(1 - i \frac{\omega}{\omega_a} \right). \quad (14)$$

³ In comparison, Mac Low et al. (1995) achieved comparable accuracy as ours using 5 and 10 cells per L , Choi et al. (2009) achieved similar or better accuracy at 6.4 cells per L .

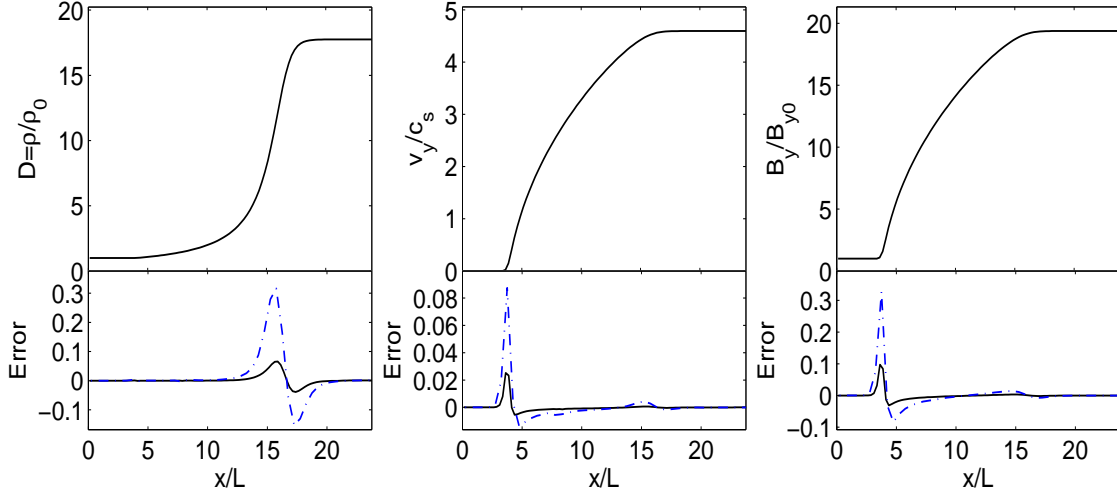


FIG. 1.— The profile of a C-type shock with $M = 50$, $A = 10$ and $\theta = \pi/4$. The upper panels show the semi-analytical solution of gas density ρ , perpendicular velocity v_y and perpendicular magnetic field B_y . ρ and B_y are normalized to their upstream values, and v_y is normalized to the sound speed. The lower panels show the corresponding absolute errors (same units as the upper panels) from our numerical simulations, with resolutions of 4 cells per L (black solid) and 2 cells per L (blue dash-dotted).

where $\omega_a \equiv \gamma \rho_i$, v_A is the Alfvén velocity, θ is the angle between the magnetic field and the wave vector. The damping rate of fast and slow waves can be obtained by solving the quadratic equation

$$(\omega^2 - v_f^2)(\omega^2 - v_s^2) + i(\omega^2 - k^2 c_s^2)k^2 v_A^2 \frac{\omega}{\omega_a} = 0, \quad (15)$$

where v_f and v_s are the fast and slow magnetosonic speeds.

When $\omega \ll \omega_a$, the damping rate is small and can be found by expanding the ideal MHD dispersion relation to powers of ω/ω_a , and to the first order, we find for the damping rate of the Alfvén wave

$$\Gamma_A = \frac{1}{2} \frac{k^2 v_A^2 \cos^2 \theta}{\omega_a}. \quad (16)$$

The damping rate for fast and slow magnetosonic waves are

$$\Gamma_f = \frac{1}{2} \left(\frac{v_f^2 - c_s^2}{v_f^2 - v_s^2} \right) \frac{k^2 v_A^2}{\omega_a}, \quad \Gamma_s = \frac{1}{2} \left(\frac{c_s^2 - v_s^2}{v_f^2 - v_s^2} \right) \frac{k^2 v_A^2}{\omega_a}. \quad (17)$$

We perform the linear wave damping test in 1D, 2D and 3D. In 1D, the wave is grid-aligned, whose wave length equals 1 in code unit. In 2D and 3D test problems, the wave vectors are not grid-aligned, with box sizes chosen such that the wave length is also 1 [in 2D, the box size is $(\sqrt{5}, \sqrt{5}/2)$ and in 3D, the box size is $(3, 1.5, 1.5)$]. We use isothermal equation of state with $c_s = 1$. The background gas density is $\rho_0 = 1$. As before, we choose $\nu = 0$. In 1D, the wave vector is along the x direction, and the adopted magnetic field is $B_{0x} = 1.0$, $B_{0y} = \sqrt{2}$ and $B_{0z} = 0.5$. In 2D and 3D the background magnetic field vector is rotated with the wave vector accordingly while keeping θ the same as in 1D (and a vector potential is used to initialize the wave in order to preserve the divergence free condition). From the above we get $v_A = \sqrt{13/4}$, $v_f = 2$ and $v_s = 1/2$, therefore we find $\Gamma_A = 2\pi^2 Q_A$, $\Gamma_f = 5.2\pi^2 Q_A$ and $\Gamma_s = 1.3\pi^2 Q_A$.

In practice, we adopt $\omega_a = 100$ and run our simulation to $t = 5$. By default, the grid size is 32 in 1D, 64×32 in 2D, and $64 \times 32 \times 32$ in 3D. Accounting for the box size in each dimension, the effective resolution, characterized by number of cells per wavelength, is 32, 28.6 and 21.3 in 1D, 2D and 3D respectively. The results are shown in Figure 2. From left to right, we show the damping curve from 1D, 2D and 3D simulations in the solid lines, where black, blue and red lines label Alfvén, fast and slow MHD waves. Dashed lines show the theoretical damping curve. We see that the numerical damping rate matches very well with the theoretical damping rate. In the 3D runs, the damping rate for the Alfvén wave is slightly faster than expected, but this may be because the effective resolution is less.

We have also run the simulations with double and half the resolution. With double resolution, the numerical damping curves in 1D, 2D and 3D cases almost match exactly the analytical damping curves (besides some small oscillations due to the initial conditions). At half resolution, however, the numerical damping rate deviates substantially (about 15% to 30% at $t = 5$). These results indicate that at least 20 cells per wavelength is need to accurately capture the effect of AD.

3. SIMULATIONS AND RESULTS

In this section we describe three groups of simulations and study the effect of AD on the non-linear evolution of the MRI. All our simulations are vertically unstratified by ignoring the disk vertical gravity with fixed box height to be one disk scale height $H = c_s/\Omega$. We initialize our simulations with Keplerian velocity and seed density perturbations of 2.5% of the background density ρ_0 . We consider three different magnetic field geometries (net vertical flux, net toroidal flux, both vertical and toroidal flux) as described in the following three subsections. Since all our simulations contain net magnetic flux, they are not subject to the issue of convergence found by (Fromang & Papaloizou 2007) in zero net-flux simulations, and numerical convergence is confirmed in

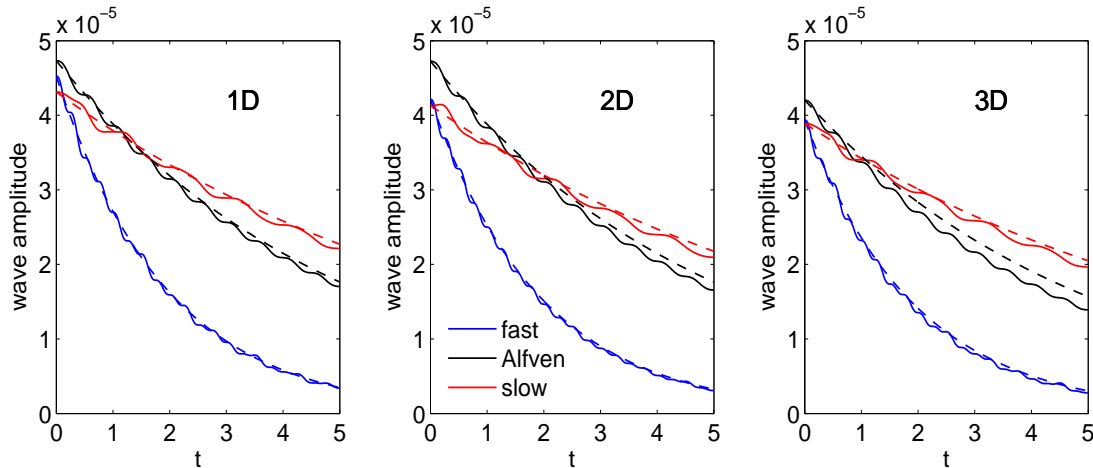


FIG. 2.— The damping of linear MHD waves by ambipolar diffusion. Three panels from left to right show the test results for 1D, 2D and 3D, where in the latter two cases the waves are not grid-aligned. In each panel, black, blue and red curves show the damping of Alfvén, fast and slow waves respectively. Solid lines are the measured damping curve, while dashed lines are the expected damping curve.

our test simulations (and see Section 3.2.2 for the case of net toroidal flux). For relatively small AD coefficient (large Am), MRI grows quickly from the seed perturbations and saturates into turbulence; when the effect of AD is strong, however, MRI does not grow from our seed perturbations. In such cases, we initialize the simulations from a turbulent state which is obtained from simulations with relatively large Am (see individual subsections for details).

The most important diagnostics are the volume averaged (normalized) Reynolds stress, defined as

$$\alpha_{\text{Re}} = \frac{\overline{\rho v_x v'_y}}{\rho_0 c_s^2}, \quad (18)$$

where the over bar indicates volume averaging, v'_y is the azimuthal velocity with the Keplerian velocity subtracted, and the volume averaged (normalized) Maxwell stress, defined as

$$\alpha_{\text{Max}} = \frac{-\overline{B_x B_y}}{4\pi\rho_0 c_s^2}. \quad (19)$$

The total stress, namely, the α parameter (Shakura & Sunyaev 1973) is $\alpha = \alpha_{\text{Re}} + \alpha_{\text{Max}}$. We also monitor the kinetic and magnetic energy density, which characterize the strength of the MRI turbulence.

The main purpose of this study is to identify the criterion under which sustained turbulence generated by the MRI can be maintained. However, the term “sustained turbulence” is a somewhat ambiguous concept. In the context of 3D shearing box simulations, small-amplitude oscillations left from decayed hydrodynamical turbulence is present (Shen et al. 2006). Such oscillations produce Reynolds stress on the order of 10^{-4} with kinetic energy density on the order of 10^{-3} , both in normalized unit $\rho_0 c_s^2$. Such oscillations are likely to associate with linear modes in the shearing sheet with the origin of acoustic and/or nearly incompressible inertia waves (Balbus 2003). Being a conservative Godunov MHD code, the Athena code preserves the amplitude of these waves without much damping. Therefore, throughout this paper, the level of turbulence we are interested

in are those whose time and volume averaged kinetic energy density $E_k = \langle \rho v^2 \rangle$ is on the order of $10^{-3} \rho_0 c_s^2$ or higher, and/or whose total stress α is no less than 10^{-4} . Meanwhile, analysis of all our simulations show that the threshold where the MRI turbulence can be marginally self-sustained is roughly at the same level. (see Section 3.2.4 for further discussion).

Our simulations are run for at least 24 orbits ($150\Omega^{-1}$). A period of 24 orbits is sufficiently long for the MRI to saturate from initial growth, which typically occurs in 5 – 10 orbits, or for the restart runs to reach a steady state, which typically occurs in 10 – 15 orbits. Our time averaged quantities are mostly taken from after about 16 orbits (since $100\Omega^{-1}$) unless otherwise noted. Although a time average over 8 orbits ($50\Omega^{-1}$) is relatively short, it is sufficient for our purpose to judge whether MRI turbulence can be self-sustained⁴. Many of our simulations are run for 48 orbits or longer where better statistics on the turbulence properties can be obtained.

3.1. Net Vertical Flux Simulations

In the first group of simulations, we choose the initial field configuration to be uniform along the vertical axis \hat{z} , characterized by the plasma $\beta_0 = 2P_0/B_0^2$, where $P_0 = \rho_0 c_s^2$ is the background pressure and B_0 is the initial field strength. The vertical flux is conserved numerically by remapping the toroidal component of the magnetic field in the ghost zones of the radial boundaries (see Section 4 of Stone & Gardiner (2010) for details). For all simulations, we fix the box size to be $4H \times 4H \times H$ in the radial, azimuthal and vertical dimensions, with fixed grid resolution at 64 cells per H . We have chosen a relatively large radial box size ($4H$), as suggested by Pessah & Goodman (2009), which is needed to prop-

⁴ Winters et al. (2003) found that more than a few hundred orbits as are required to accurately measure the properties of the MRI turbulence in ideal MHD. This conclusion is based simulations with radial box size being H , while the radial box size in about half of our simulations is $4H$, which reduces the time fluctuations. Also, our Figures 3 and 8 show that the fluctuations in the Maxwell stress are less severe in the presence of AD than in the ideal MHD case.

erly capture the parasitic modes to break the channel mode into turbulence. It also help substantially reduce the intermittence of the MRI turbulence (Bodo et al. 2008). We note that for local unstratified net vertical flux MRI simulations without explicit dissipation, turbulence properties converge at about 32 cells per H (Hawley et al. 1995). The grid resolution in our simulations is two times higher, thus we expect numerical convergence.

All our net vertical flux simulations are listed in Table 1. We first perform a fiducial set of simulations with fixed $\beta_0 = 400$. We choose a series of Am values, ranging from 1000 down to 0.1, and study the critical value of Am below which MRI turbulence is no longer self-sustained (Section 3.1.1). In the next, we vary the net vertical flux by setting $\beta_0 = 100, 1600$ and 10^4 and run a number of simulations around $Am = 1$ to study how the critical value of Am is affected by the vertical flux (Section 3.1.2). Moreover, in Section 3.1.3 we briefly investigate the effect of ν by varying ν from the fiducial value 0.5 to 0 (run Z5a) and 1 (run Z5b) (see equation (4)). Finally, we discuss the properties of the MRI turbulence in the presence of AD (Section 3.1.4).

Our choices of the net vertical flux derive from the linear dispersion relation of the MRI as well as physical considerations. In the case of ideal MHD, the wavelength for the fastest growing linear MRI mode is given by $\lambda/H = 9.18\beta_0^{-1/2}$ (Hawley et al. 1995). For $\beta_0 = 100, 400$ and 1600 , our vertical box size of H fits 1, 2 and 4 most unstable wavelengths respectively in ideal MHD. The ideal MHD dispersion relation is considerably modified when $Am \lesssim 10$. Unstable modes exist for wavelength longer than the critical wavelength (Wardle 1999)

$$\frac{\lambda_c}{H} = 5.13 \left(1 + \frac{1}{Am^2} \right)^{1/2} \beta_0^{-1/2}. \quad (20)$$

The wavelength for the most unstable mode λ_m is about twice larger. An approximate fitting formula that is accurate within 2% for all values of Am is

$$\frac{\lambda_m}{H} \approx 10.26 \left(1 + \frac{1}{Am^2} + \frac{1}{Am^{1.16\epsilon}} - 0.2\epsilon \right)^{1/2} \beta_0^{-1/2}, \quad (21)$$

where $\epsilon \equiv Am/(1 + Am)$. Note that for pure vertical magnetic field and vertical wavenumber, the linear dispersion relation for Ohmic resistivity is exactly the same as that for AD (Wardle 1999), with Am replaced by the Elsasser number $\Lambda = v_{Az}^2/\eta\Omega$. For $\beta_0 = 400$, the most unstable wavelengths at $Am = 1, 1/3$ and 0.1 are $\lambda = 0.87H, 1.72H$ and $5.18H$ respectively. Clearly, the most unstable mode does not fit into our simulation box when $Am = 0.33$, and no unstable modes fit into the box for $Am = 0.1$. Since $\lambda \propto \beta_0^{-1/2}$, these modes do fit into our simulation box as we increase β_0 to 1600 and 10^4 respectively. In the mean time, since AD tends to be important in the more strongly magnetized upper layers of the protoplanetary disks (Wardle 2007; Bai 2011), it is also interesting to study whether the MRI turbulence can be sustained when β_0 is relatively small, even if the most (or all) unstable modes do not fit into our simulation box. We have not run simulations with a taller box since we do not include vertical stratification.

TABLE 1
NET VERTICAL FLUX SIMULATIONS.

Run	Am	β_0	ν	Orbits	Restart ¹	Turbulence ²
Z1	1000	400	0.5	48	No	Yes
Z2	100	400	0.5	24	No	Yes
Z3	10	400	0.5	24	No	Yes
Z4	3.33	400	0.5	24	No	Yes
Z5	1	400	0.5	43	No	Yes
Z6	0.33	400	0.5	24	Z5	No
Z7	0.1	400	0.5	24	Z5	No
Z3s	10	100	0.5	24	No	Yes
Z5s	1	100	0.5	24	No	Yes
Z6s	0.33	100	0.5	24	Z5s	No
Z7s	0.1	100	0.5	24	Z5s	No
Z3w	10	1600	0.5	24	No	Yes
Z5w	1	1600	0.5	24	No	Yes
Z6w	0.33	1600	0.5	48	No	Yes
Z7w	0.1	1600	0.5	24	Z5w	No
Z6e	0.33	10^4	0.5	48	No	Yes
Z7e	0.1	10^4	0.5	48	Z6e	Yes
Z5a	1	400	0.0	24	No	Yes
Z5b	1	400	1.0	24	No	Yes

Box size is fixed at $4H \times 4H \times H$, grid resolution is 64 cells per H .
¹ whether simulation is initiated by restarting from a turbulent run.

² whether turbulence can be self-sustained.

3.1.1. A Fiducial Set of Runs

As the fiducial set of runs, we fix $\beta_0 = 400$, and run 7 simulations with different Am values (see Table 1), labeled from Z1 with $Am = 1000$, which essentially corresponds to the ideal MHD case, to Z7 with $Am = 0.1$, where the evolution of magnetic field is dominated by AD. Our scan of Am is more narrowly sampled near $Am = 1$ where the transition is expected to occur. In Figure 3, we show the time evolution of the Maxwell stress from the fiducial set of runs. We find that for $Am \geq 1$, the growth of the MRI from linear perturbations leads to vigorous MRI turbulence, while for the two runs with $Am < 1$, MRI either does not grow from the initial vertical field (Z7), or grows too slowly (Z6), since the most unstable modes do not fit into our simulation box. Therefore, for these two models, we start the simulations from the end of run Z5 ($Am = 1$), which is turbulent, and reset Am to be 0.33 and 0.1 respectively. Nevertheless, turbulence continues to decay throughout the span of our simulation in run Z7. Run Z6 is a marginal case where turbulence is neither fully sustained nor decayed continuously (see discussions below).

We first look at run Z1 to Z5 with $Am \geq 1$. The initial growth of the MRI is due to the axisymmetric channel mode (Goodman & Xu 1994; Pessah & Chan 2008). The mode becomes non-linear (producing an overshoot in the Maxwell stress up to 1 in the ideal MHD case) until broken down by secondary parasitic modes to produce turbulence. In the turbulent state, it is evident that the Maxwell stress monotonically decreases as Am decreases, analogous to the Ohmic case (Sano et al. 1998; Fleming et al. 2000). In Table 2 we list the general properties of the turbulence from all our vertical net flux simulations. The quantities are averaged over space and time after saturation (after $100\Omega^{-1}$). The total stress $\alpha \approx 0.2$ in run Z1, which agrees with the ideal MHD

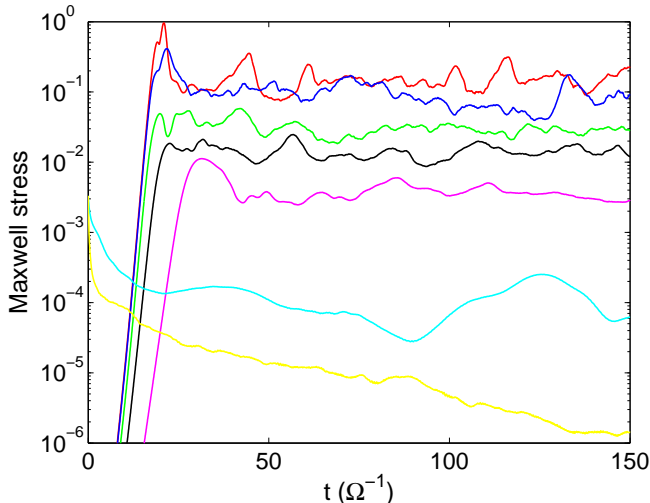


FIG. 3.— The evolution of Maxwell stress in our fiducial set of net vertical flux runs (from top to bottom: Z1, Z2, ..., Z7) normalized to $c_s H$. For models Z6 and Z7, the simulations are initiated from the end of run Z5.

case (Hawley et al. 1995). It drops slowly with decreasing Am when $Am \gg 1$, but very rapidly when Am is around 1. Moreover, as Am decreases, the ratio of kinetic to the fluctuating part (with background field B_{z0} subtracted) of the magnetic energy increases (see also Figure 5). Similarly, the ratio of Reynolds stress to Maxwell stress increases.

As we have discussed before, the most unstable mode does not fit into our simulation box for runs Z6 and Z7, and our simulations initiated from a turbulent state also show no sign of sustained MRI turbulence. This is not surprising for run Z7, where no unstable MRI mode even exists in the simulation box. Our run Z6 is a marginal case, where a wavelength of H is only slightly larger than the critical wavelength for instability ($\lambda_c = 0.89H$) but far from the most unstable wavelength ($\lambda_m = 1.72H$). This explains the long-term variations in the Figure 3 since the growth rate is only slightly larger than zero. Our analysis in Section 3.2.4 indicates that although some non-zero stress close to $\alpha = 10^{-4}$ is maintained in the simulation, it is unlikely to be due to the MRI turbulence. In real disks, one may expect sustained turbulence to be supported at $Am \approx 0.3$ if it were at the disk midplane, where the density variation over one H above and below the midplane is not significant. In the upper layers, β_0 may fall off substantially over one H , which strongly stabilizes the flow. In sum, we see from our fiducial set of net vertical flux simulations that presence of turbulence mainly depends on whether the most unstable mode of the MRI fits into the simulation box. This aspect will be further explored in the next subsection 3.1.2.

The results reported above are qualitatively different from those observed in HS using two-fluid simulations. One may compare our results with Table 3 of HS, where the Am value for their four runs Z24, Z17, Z25, Z28 are 0.11, 1.1, 11.1 and 111 respectively. The total stress α in these simulations does not scale monotonically with Am , and in particular α is on the order of 10^{-2} when Am is as small as 0.11, while in our simulations MRI is suppressed.

This reflects the difference in the physical assumptions about the two approaches. In the two-fluid limit, ions are coupled to the neutrals only via collisions. When the ion-neutral collisions are infrequent ($Am < 1$), the ions and neutrals behave as independent fluid: vigorous MRI is generated in the ion fluid while the neutrals remain quiescent, and the overall α is proportional to the ion fraction $f = \rho_i/\rho$. In the strong-coupling limit, the ions and the neutrals are coupled not only by collisions, but also via the ionization-recombination reactions. Since the strong-coupling limit requires the recombination time to be much smaller than the orbital time, this means that ions are continuously created and destroyed on a time scale that is much shorter than the time scale for MRI to grow. It is this additional chemical coupling that quenches the MRI in the ion fluid, and suppresses angular momentum transport for $Am \lesssim 0.1$.

3.1.2. The Effect of Vertical Field Strength

We select a number of models from the fiducial series and rerun the simulations with three additional initial β_0 values: $\beta_0 = 100, 1600$ and 10^4 (e.g., with magnetic field strength two times and half of that in the fiducial models, as well as one case with an very weak field). These simulations are labeled with an additional letter “s” (for strong), “w” (for weak) and “e” (for extremely weak) in Table 1. For strong field simulations with $\beta_0 = 100$, the wavelength for the fastest growing mode exceeds the vertical box size when $Am < 10$. When $Am < 1$, there are essentially no unstable mode in the simulation box. Runs Z3s and Z5s are initiated from seed perturbations, while runs Z6s and Z7s are initiated from the turbulent state at the end of run Z5s. For weak field runs with $\beta_0 = 1600$, on the other hand, the most unstable mode can be fitted into the simulation box for all runs with $Am \gtrsim 0.3$. No unstable mode is fitted into the simulation box when $Am = 0.1$, and as before, Run Z7w is initiated from turbulent state from Z5w to test whether turbulence can be sustained. Our $\beta_0 = 10^4$ simulations allows the most unstable wavelength to be fitted in the simulation box at small Am . We conduct two runs in this case with $Am = 0.33$ (Z6e) and $Am = 0.1$ (Z7e). Run Z7e is initialized from the turbulent state in Z6e to avoid the extremely long time in the linear growth stage. Time averaging in runs Z6w, Z6e and Z7e are taken since $t = 200\Omega^{-1}$ (time averaging in other runs are taken since $t = 100\Omega^{-1}$ by default).

We find from our simulations that sustained MRI turbulence is present in all models except Z6s, Z7s and Z7w. In particular, the MRI turbulence can be self-sustained even the Am value is as small as 0.1, provided that the net vertical field is sufficiently weak. These results confirm our speculation in the fiducial set of simulations that the MRI turbulence is self-sustained as long as unstable MRI modes fit into the simulation box.

The diagnostic quantities from time and volume averaged quantities in the turbulent state from the weak and strong field series of runs are also listed in Table 2. We see that for $Am = 10$, the averaged kinetic energy, Reynolds and Maxwell stress monotonically decreases with increasing β_0 . Although not all our simulations are not run long enough for these quantities to be measured accurately, the trend is significant enough and indicates that

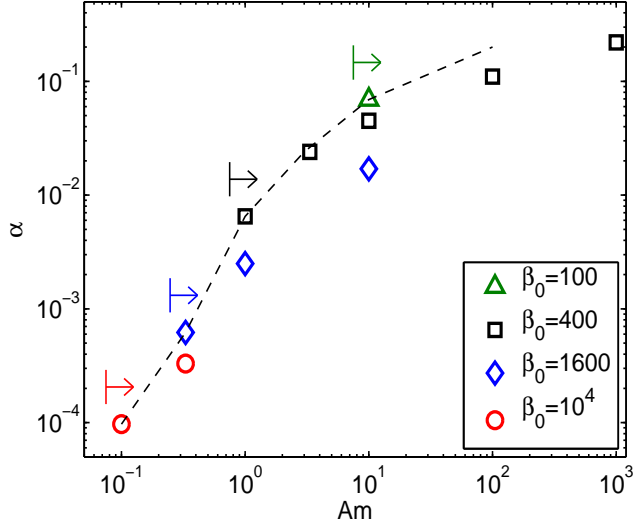


FIG. 4.— The time and volume averaged total stress α from all our net vertical flux simulations that sustain MRI turbulence. Simulations with different net vertical flux, characterized by the plasma β_0 , are labeled by different symbols and colors. The arrows above the symbols indicate (for each β_0 as represented by the symbol) the range of Am where the most unstable wavelength is smaller than H . The dashed line connecting the symbols represents the maximum value of stress attainable from net vertical flux simulations.

the MRI saturate at a higher level with higher net vertical flux (small β_0), in agreement with the ideal MHD case (Hawley et al. 1995). For $Am = 1$, the monotonicity trend is still present by comparing our fiducial run Z5 and the weak field run Z5w. The saturation level of the MRI turbulence in the strong field run Z5s is weaker than that for run Z5. This is most likely because the most unstable mode does not fit into our simulation box (but some less unstable modes fit) in run Z5s. The monotonicity trend further preserves at $Am = 0.33$, where the kinetic energy density and total stress from run Z6w is larger than those from run Z6e by about a factor of 2.

We summarize the main results from the net vertical flux simulations in Figure 4. Shown are the total stress α from all the simulations that the most unstable mode is properly resolved so that the MRI turbulence is self-sustained and a reliable value of α can be obtained. As discussed before, at a fixed β_0 , there exists a critical value of Am below which the most unstable wavelength would exceed H and the mode tend to be suppressed due to the vertical stratification. This is effect is illustrated by the colored arrows in the Figure. Equivalently, for turbulence to be sustained at small Am , β_0 must be sufficiently large $\beta_0 \gtrsim 100/Am^2$, as can be obtained from equation (21). At a given Am , since the stress α monotonically increases with the net vertical flux, there exist a maximum stress, corresponding to the largest allowed net flux (smallest allowed value of β_0). This maximum value of α as a function of Am is illustrated in the dashed line by connecting results from runs Z7e, Z6w, Z5 and Z3s. We see that the maximum α drops by a factor of about 40 from the ideal MHD case to $Am = 1$, and another factor of about 60 as Am decreases to 0.1. By extrapolating this trend, we expect the MRI turbulence can be self-sustained for arbitrarily small value of Am ,

as long as the background magnetic field is sufficiently weak. Nevertheless, the turbulence would seem to be too weak ($\alpha < 10^{-4}$) to produce significant amount of angular momentum transport as required by most astrophysical disks.

3.1.3. The Effect of ν

The parameter ν reflects the sensitivity of how the AD coefficient depends on gas density (see Equation (4)). Most of our simulations are run with fixed value of $\nu = 0.5$, while ν can in principal span a range from 0 to 1. The significance about the effect of ν largely depends on the level of density fluctuation in the MRI turbulence. In Table 2, we list the rms density fluctuation relative to the background gas density from all vertical net flux runs (see column $\langle \delta\rho \rangle / \rho_0$). The rms density fluctuation in the ideal MHD case (run Z1) is relatively large, up to 0.3, and the largest and smallest densities reach about 0.2 and 4 times the background density. Since AD reduces the saturation level of the MRI turbulence, the density fluctuations become smaller as Am decreases. This fact undermines the importance of ν : when the effect of ν may be important (large density fluctuations), AD only plays an insignificant role in the MRI turbulence (large Am); when AD strongly affect the MRI turbulence (small Am), the density fluctuation becomes much smaller and ν is much less likely to be important. This above implies that variations in the value of ν should not have a major impact, and in particular, the critical value of Am below which MRI is suppressed is unlikely to be altered by different choices of ν .

To confirm our expectations, we perform two additional runs with the same initial conditions as run Z5 ($Am = 1$, $\beta_0 = 400$), but set ν to be 0 and 1 respectively. These two runs are named Z5a and Z5b. We see from Table 2 that the turbulence properties from these two runs are essentially identical to those in run Z5. Even though our time averages are taken over relatively short periods, the deviations are generally within 10%. This is understandable since the density fluctuations in these runs are as small as 0.07. It appears certain that the value of ν only plays a very minor role in the MRI turbulence in the strong coupling limit.

3.1.4. Properties of the MRI turbulence with AD

Besides the general properties of the MRI turbulence listed in Table 2, we study two other aspects of the MRI turbulence with AD.

First, we study the power spectrum density (PSD) of magnetic and kinetic energies by Fourier analysis. The Fourier analysis in the shearing periodic system is performed by the remapping technique before and after Fourier transformation, as described in Section 2.4 of Hawley et al. (1995). Although the PSD is anisotropic in k -space, it would be beneficial to plot the PSD in one dimensional form by some averaging procedure. Following Davis et al. (2010), we compute shell-integrated power spectrum of the magnetic field $B_k^2 \equiv 4\pi k^2 |\tilde{\mathbf{B}}(k)|^2$, where $|\tilde{\mathbf{B}}(k)|^2$ denotes the average of $|\tilde{\mathbf{B}}(\mathbf{k})|^2$ over shells of constant $k = |\mathbf{k}|$, and $\tilde{\mathbf{B}}(\mathbf{k}) = \int \mathbf{B}(\mathbf{x}) e^{-i\mathbf{k}\cdot\mathbf{x}} d^3\mathbf{x} / V$ is the Fourier transform of $\mathbf{B}(\mathbf{x})$. Here V is the volume of the simulation box. The Fourier transformation is of

TABLE 2
TIME AND VOLUME AVERAGED QUANTITIES IN NET VERTICAL FLUX SIMULATIONS.

Run	$E_{k,x}$	$E_{k,y}$	$E_{k,z}$	E_k	$E_{M,x}$	$E_{M,y}$	$E_{M,z}$	$\langle \delta \rho \rangle / \rho_0$	α_{Re}	α_{Max}	α
Z1	7.0×10^{-2}	0.10	2.9×10^{-2}	0.20	8.4×10^{-2}	0.20	3.4×10^{-2}	0.36	5.4×10^{-2}	0.17	0.22
Z2	4.4×10^{-2}	6.5×10^{-2}	1.9×10^{-2}	0.13	4.5×10^{-2}	8.7×10^{-2}	2.1×10^{-2}	0.31	3.3×10^{-2}	7.4×10^{-2}	0.11
Z3	2.8×10^{-2}	2.7×10^{-2}	1.4×10^{-2}	6.9×10^{-2}	1.4×10^{-2}	3.3×10^{-2}	9.9×10^{-3}	0.20	1.6×10^{-2}	2.9×10^{-2}	4.5×10^{-2}
Z4	1.8×10^{-2}	1.3×10^{-2}	8.6×10^{-3}	4.0×10^{-2}	6.5×10^{-3}	1.8×10^{-2}	6.3×10^{-3}	0.14	9.0×10^{-3}	1.5×10^{-2}	2.4×10^{-2}
Z5	5.4×10^{-3}	1.9×10^{-3}	3.1×10^{-3}	1.0×10^{-2}	1.2×10^{-3}	5.1×10^{-3}	3.3×10^{-3}	0.070	2.4×10^{-3}	4.1×10^{-3}	6.5×10^{-3}
Z3s	3.5×10^{-2}	3.3×10^{-2}	9.6×10^{-3}	7.8×10^{-2}	3.4×10^{-2}	5.0×10^{-2}	2.7×10^{-2}	0.18	2.9×10^{-2}	4.0×10^{-2}	6.9×10^{-2}
Z5s	3.7×10^{-3}	1.8×10^{-3}	3.5×10^{-3}	9.0×10^{-3}	1.2×10^{-3}	1.2×10^{-3}	1.0×10^{-2}	0.063	2.4×10^{-3}	2.2×10^{-3}	4.6×10^{-3}
Z3w	1.0×10^{-2}	7.3×10^{-3}	4.6×10^{-3}	2.2×10^{-2}	4.4×10^{-3}	2.0×10^{-2}	3.6×10^{-3}	0.091	5.1×10^{-3}	1.2×10^{-2}	1.7×10^{-2}
Z5w	2.5×10^{-3}	1.1×10^{-3}	9.6×10^{-4}	4.6×10^{-3}	3.6×10^{-4}	3.5×10^{-3}	1.1×10^{-3}	0.054	9.5×10^{-4}	1.5×10^{-3}	2.5×10^{-3}
Z6w	9.3×10^{-4}	2.0×10^{-4}	5.8×10^{-4}	1.7×10^{-3}	5.3×10^{-5}	7.7×10^{-4}	7.2×10^{-4}	0.037	2.9×10^{-4}	3.3×10^{-4}	6.2×10^{-4}
Z6e	7.0×10^{-4}	1.5×10^{-4}	7.7×10^{-5}	9.2×10^{-4}	2.1×10^{-5}	4.7×10^{-4}	1.5×10^{-4}	0.036	2.1×10^{-4}	1.2×10^{-4}	3.3×10^{-4}
Z7e	2.8×10^{-4}	5.3×10^{-5}	3.4×10^{-5}	3.7×10^{-3}	4.3×10^{-6}	1.3×10^{-4}	1.2×10^{-4}	0.023	6.6×10^{-5}	3.1×10^{-5}	9.7×10^{-5}
Z5a	5.4×10^{-3}	2.0×10^{-3}	3.3×10^{-3}	1.1×10^{-2}	1.2×10^{-3}	5.2×10^{-3}	3.3×10^{-3}	0.070	2.4×10^{-3}	4.1×10^{-3}	6.4×10^{-3}
Z5b	5.0×10^{-3}	1.8×10^{-3}	3.3×10^{-3}	1.0×10^{-2}	1.4×10^{-3}	4.9×10^{-3}	3.3×10^{-3}	0.068	2.2×10^{-3}	3.8×10^{-3}	6.0×10^{-3}

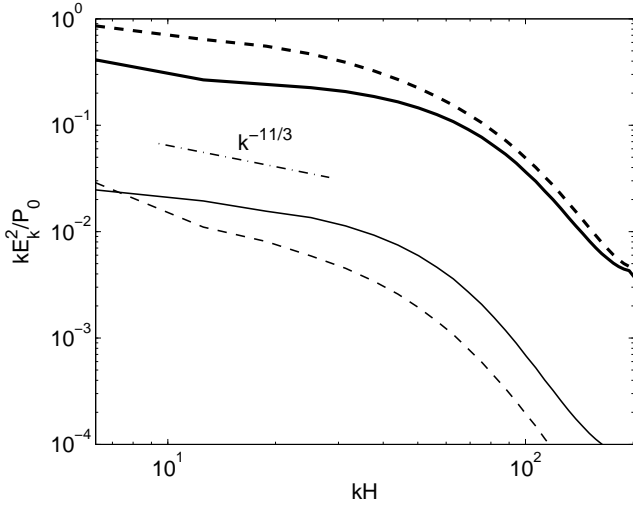


FIG. 5.— The power spectrum density of the kinetic (solid) and magnetic (dashed) energy densities, for two vertical net flux simulations with $Am = 1000$ (run Z1, bold) and $Am = 1$ (run Z5, thin). Plotted are the shell integrated spectrum, represented by $E_k^2 = 4\pi k^2 |\tilde{E}(k)|^2$ (where E denotes kinetic or magnetic energy density), normalized to background pressure $P_0 = \rho_0 c_s^2$. The area enclosed by each curve corresponds to the total energy density from turbulent fluctuations.

course discrete, but for notational convenience we write the formulas in continuous form. According to Parseval's theorem, we have

$$\begin{aligned} \frac{1}{V} \int_V |\mathbf{B}(\mathbf{x})|^2 d^3\mathbf{x} &= \int |\tilde{\mathbf{B}}(\mathbf{k})|^2 \frac{d^3\mathbf{k}}{(2\pi)^3} \\ &= \frac{1}{(2\pi)^3} \int 4\pi k^2 |\tilde{\mathbf{B}}(k)|^2 dk. \end{aligned} \quad (22)$$

Dividing by a factor of 8π we obtain the PSD for the magnetic energy density $M_k = B_k^2/8\pi$. Similarly, one can obtain the PSD for the kinetic energy K_k .

In Figure 5, we show the PSDs computed from our runs Z1 and Z5. These two simulations are representative for the MRI turbulence in the ideal MHD and AD dominated regimes respectively, and are run for two times

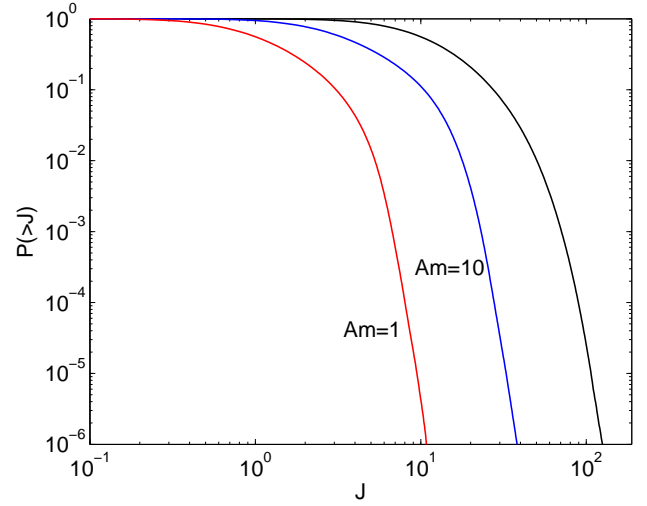


FIG. 6.— Cumulative probability distribution of current density J for our simulations Z1 ($Am = 1000$, black), Z3 ($Am = 10$, blue), Z5 ($Am = 1$, red). The current is normalized to $\sqrt{4\pi P_0 c}/4\pi H$.

longer than many other simulations (thus giving better statistics). We see that the shape of the PSD obtained from our simulations are very similar. The PSD roughly follows a power-law form at small k , with the power law index approximately equals to $-11/3$, which is the index for incompressible Kolmogorov turbulence spectrum. There appears to be a spectral break at $kH \approx 70$, corresponding to a wavelength of about $0.1H$, and the PSD falls off rapidly toward smaller scales. The turbulent power in the $Am = 1$ case is about 20 times smaller than that in the ideal MHD case. Magnetic energy fluctuations dominate kinetic energy fluctuations in the ideal MHD case, while in the AD dominated regime, more turbulence power resides in the kinetic energy. Moreover, we have also checked the contour plot of vertically integrated PSD (not shown) and found that the turbulence becomes more anisotropic in the AD dominated regime: the turbulent power is more elongated in k_x than in k_y .

Second, we study the effect of AD on the distribution of current in the MRI turbulence. It has been shown that in

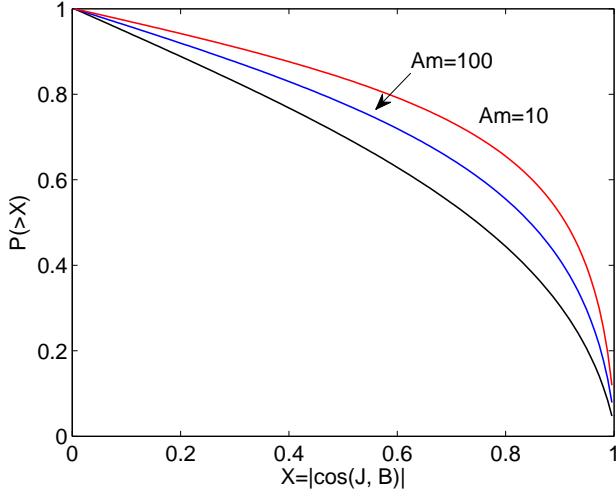


FIG. 7.— Cumulative probability distribution of $|\cos \alpha|$, where α is the angle between \mathbf{J} and \mathbf{B} . Shown are the results from our runs Z1 ($Am = 1000$, black), Z2 ($Am = 100$, blue), Z3 ($Am = 10$, red).

one and two dimensions, sharp current structure can be developed around magnetic nulls in the presence of AD (Brandenburg & Zweibel 1994). To examine whether the same effect is present in the MRI turbulence, we show in Figure 6 the cumulative probability distribution of the current density $J = |\mathbf{J}|$ in our simulation runs Z1, Z3 and Z5. If sharp current structure were to form, one would expect to see extended tails in the probability distribution. However, we see that as Am decreases, the probability distribution shifts leftward since turbulence becomes weaker, but its shape remains largely unchanged. We also note that the current sharpening phenomenon is not observed in simulations by (Brandenburg et al. 1995) either. It is likely the sharpening of current by AD is overwhelmed in 3D MHD turbulence.

AD has also been shown to tend to reduce the current component that is perpendicular to the magnetic field (Brandenburg et al. 1995) and make the magnetic configuration more force-free. To examine this effect, we show the cumulative probability distribution of $|\cos \alpha|$ from our simulation runs Z1, Z2 and Z3 in Figure 7, where α is the angle between the current and the magnetic field. The cumulative distribution functions from our runs Z4 and Z5 are almost identical to that from run Z3, where $Am = 10$. We confirm that AD makes the distribution more concentrated toward $|\cos \alpha| = 1$ (i.e., $\mathbf{J} \parallel \mathbf{B}$).⁵ Nevertheless, since the distribution of $|\cos \alpha|$ is already peaked at 1 in the essentially ideal MHD run (Z1), the effect of AD does not modify the distribution of current orientation substantially.

3.2. Net toroidal flux simulations

⁵ We also report a difference in our results from Brandenburg et al. (1995). In their simulations, the distribution function peaks at $|\cos \alpha| = 0$ in ideal the MHD case, and AD concentrate the current toward $|\cos \alpha| = 1$. In our simulations, we find that the distribution function is already concentrated at $|\cos \alpha| = 1$ under ideal MHD, and AD simply makes it more concentrated.

TABLE 3
NET TOROIDAL FLUX SIMULATIONS.

Run	Am	β_0	Resolution	Restart	Turbulence
Y1	1000	100	$64 \times 128 \times 64$	No	Yes
Y2	100	100	$64 \times 128 \times 64$	No	Yes
Y3	10	100	$64 \times 128 \times 64$	Y1	Yes
Y4	3.33	100	$64 \times 128 \times 64$	Y1	Yes
Y5	1	100	$64 \times 128 \times 64$	Y1	No
Y6	0.33	100	$64 \times 128 \times 64$	Y1	No
Y7	0.1	400	$64 \times 128 \times 64$	Y1	No
Y1w	1000	100	$64 \times 128 \times 64$	No	Yes
Y2w	100	100	$64 \times 128 \times 64$	No	Yes
Y3w	10	400	$64 \times 128 \times 64$	Y1w	Yes
Y4w	3.33	400	$64 \times 128 \times 64$	Y1w	Yes
Y5w	1	400	$64 \times 128 \times 64$	Y1w	No
Y6w	0.33	400	$64 \times 128 \times 64$	Y1w	No
Y7w	0.1	400	$64 \times 128 \times 64$	Y1w	No
Y1h	1000	100	$128 \times 256 \times 128$	No	Yes
Y3h	10	100	$128 \times 256 \times 128$	Y1h	Yes
Y5h	1	100	$128 \times 256 \times 128$	Y1h	No
Y6h	0.33	100	$128 \times 256 \times 128$	Y1h	No

Box size is fixed at $H \times 4H \times H$, ν is fixed at 0.5. All simulations are run for 24 orbits ($150\Omega^{-1}$).

In the second group of simulations, the initial field configuration is chosen to be uniform along the azimuthal direction \hat{y} , with strength characterized by $\beta_0 = 2P_0/B_0^2$, where B_0 is the initial field strength. Following Simon & Hawley (2009), we fix the box size to be $H \times 4H \times H$ in the radial, azimuthal and vertical dimensions for all simulation runs in this group⁶. We choose the fiducial resolution to be 64 cells per H in the radial and vertical direction, and 32 cells per H in the azimuthal direction. All our net toroidal flux simulations are listed in Table 3, including one set of fiducial simulations with $\beta_0 = 100$, one set of higher resolution simulations, and one set of weak field simulations with $\beta_0 = 400$. Unlike net vertical flux, the net toroidal flux is not precisely conserved in our shearing box simulations. As discussed in (Simon & Hawley 2009), ensuring strict conservation of toroidal flux numerically is more complex, and is also less important than conserving net vertical flux because the saturation level of the MRI turbulence is not very sensitive to the toroidal flux. Throughout all our simulations in this group, we find that the deviation of net toroidal flux from the initial value is generally less than 2%.

The linear stability of Keplerian disks in the presence of pure toroidal field is more complex than that for the vertical field case. It requires consideration of non-axisymmetric perturbations (Balbus & Hawley 1992), and involves the time-dependent amplification of wave modes as the radial wave number swings from leading to trailing. In ideal MHD, pure toroidal MRI favors high k_z wave numbers, and requires relatively large numerical resolution. In the case of Ohmic resistivity, swing amplification of modes is suppressed when the diffusion time of the mode is comparable to the orbital frequency (Papaloizou & Terquem 1997). A linear sta-

⁶ We have also performed our run series Y1 to Y6 using a larger box $4H \times 4H \times H$ and found that the turbulence properties are very similar.

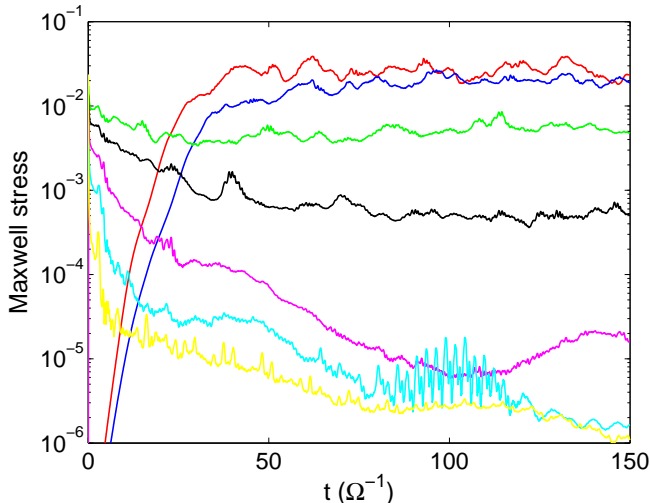


FIG. 8.— The evolution of Maxwell stress in our fiducial set of toroidal net-flux runs (from top to bottom: Y1, Y2, ..., Y7) normalized to $c_s H$. For all runs after Y2, the simulations start from the end of the Y1 run.

bility with non-axisymmetric perturbations in AD dominated regime has yet to be performed. Nevertheless, one might expect that a similar argument holds for AD, with $Am \sim 1$ as the boundary for stability.

3.2.1. A Fiducial Set of Runs

We fix $\beta_0 = 100$ and run 7 fiducial simulations with different Am values, named from Y1 with $Am = 1000$ to Y7 with $Am = 0.1$ (see Table 3) similar to the case of net vertical flux runs. Initial growth of the MRI from pure toroidal field is more difficult and is only achieved when Am is greater than 10. We initialize the rest of the simulations from the turbulent state at the end of run Y1.

Figure 8 illustrates the time evolution of the Maxwell stress from this fiducial set of runs. The time and volume averaged quantities from these runs are listed in Table 4. We find that at a given value of Am , the saturation level of the MRI with net toroidal flux is much lower than the net vertical flux case. The turbulent energy density and total stress in run Y1 (essentially ideal MHD) is a few times 10^{-2} , about an order of magnitude less than run Z1. As Am drops below 10, the saturation level of the MRI turbulence falls off very rapidly. At $Am = 3$ (run Y4), the total stress falls below 10^{-3} . At $Am = 1$, although a total stress is maintained at a level of 10^{-5} , we do not observe any signature of the MRI turbulence by examining the structure of the velocity field, which is essentially laminar (see further discussion in Section 3.2.4). Since the simulation is initialized from a turbulent state, the low level of stress and kinetic energy are mostly due to the eigen-modes of the shearing box excited from the initial turbulence, and that are not damped due to the low dissipation in the Athena code. Unlike the case for net vertical flux, there appears to exist a critical value of Am below which MRI turbulence with net toroidal flux is not self-sustained. This critical value of Am is about 3. This fact will be further discussed shortly in Section 3.2.3.

HS also performed a number of net toroidal flux two-

fluid simulations with $Am \approx 1$ and $Am \approx 100$, and in both cases turbulence is self-sustained with total stress α on the order of 10^{-4} to 10^{-3} . Again, these results are no longer valid in the strong-coupling regime and are not directly comparable to our results (see discussion in Section 3.1.1).

We see from Table 4 that the density fluctuations in the net toroidal flux simulations are generally smaller than those in the net vertical flux case. Therefore, following the discussion in Section 3.1.3, we expect the effect of ν has essentially no impact on the conclusions we have drawn above.

3.2.2. The Effect of Resolution

Relatively high resolution is needed for net toroidal flux MRI simulations in order to properly capture the amplification of wave modes as they swing from leading to trailing (Simon & Hawley 2009). In order to justify our results in the previous subsection, we perform a few of the simulations with doubled resolution. These runs are labeled with an additional letter “h” (i.e., high resolution) in Table 3.

The time and volume averaged quantities from these high resolution runs are shown in Table 4. We see that the kinetic and magnetic energy densities from in the high resolution simulations are generally larger than those in the low resolution runs, but only by a small factor. In particular, the difference between low and high resolutions with relatively large AD coefficient is only about 10% (e.g., comparing runs Y3 and Y3h), which strongly indicates numerical convergence. This is not surprising since small scale structures can be largely damped by AD thus higher resolution becomes unnecessary. Run Y5h is also very similar to run Y5, where the initial turbulence is damped with remnant small velocity and magnetic fluctuations unlikely to be associated with the MRI turbulence.

The inferences above are further justified by looking at the power spectrum of magnetic and kinetic energies. Following the same procedure described in Section 3.1.4, we show in Figure 9 the shell integrated PSDs for runs Y1, Y1h and Y3, Y3h. The spectral shapes from the low resolution simulations appear to have a spectral peak at relatively large scales of about $0.5H$, while at higher resolution, a power law spectrum at intermediate scales from approximately $0.1H$ to $0.5H$ analogous to an inertia range appears to have developed. This observation may suggest high numerical resolution of at least 128 cells per H is needed for the toroidal field MRI simulations in order to resolve the inertia range in the turbulent spectrum, although smaller resolution of 64 cells per H appears to be sufficient for turbulence properties to converge. The shape of the PSDs at small k look very different from the PSDs in the net vertical flux simulations, indicating different energy injection mechanism, while at large k , the PSDs from both cases fall off in a similar manner, indicating similar dissipation mechanism.

3.2.3. The Effect of toroidal Field Strength

We have also performed the same set of net toroidal flux simulations with the toroidal magnetic field strength lowered by one half, $\beta_0 = 400$, labeled with an additional letter “w” (i.e., weak field) in Table 3. General properties

TABLE 4
TIME AND VOLUME AVERAGED QUANTITIES IN NET TOROIDAL FLUX SIMULATIONS.

Run	$E_{k,x}$	$E_{k,y}$	$E_{k,z}$	E_k	$E_{M,x}$	$E_{M,y}$	$E_{M,z}$	$\langle \delta \rho \rangle / \rho_0$	α_{Re}	α_{Max}	α
Y1	1.2×10^{-2}	1.1×10^{-2}	5.2×10^{-3}	2.8×10^{-2}	9.7×10^{-3}	5.0×10^{-2}	4.4×10^{-3}	0.10	7.4×10^{-3}	2.6×10^{-2}	3.4×10^{-2}
Y2	1.0×10^{-2}	8.2×10^{-3}	4.6×10^{-3}	2.3×10^{-2}	8.2×10^{-3}	4.0×10^{-2}	4.0×10^{-3}	0.083	6.2×10^{-3}	2.0×10^{-2}	2.6×10^{-2}
Y3	4.6×10^{-3}	2.4×10^{-3}	1.8×10^{-3}	8.8×10^{-3}	2.4×10^{-3}	1.9×10^{-2}	1.4×10^{-3}	0.062	2.5×10^{-3}	5.7×10^{-3}	8.2×10^{-3}
Y4	6.9×10^{-4}	2.8×10^{-4}	2.1×10^{-4}	1.2×10^{-3}	3.4×10^{-4}	1.0×10^{-2}	2.4×10^{-4}	0.029	3.0×10^{-4}	5.0×10^{-4}	8.1×10^{-4}
Y5*	3.5×10^{-5}	8.2×10^{-5}	1.8×10^{-5}	1.4×10^{-4}	1.4×10^{-5}	9.7×10^{-3}	3.1×10^{-5}	0.008	6.6×10^{-6}	1.2×10^{-5}	1.9×10^{-5}
Y1w	7.3×10^{-3}	5.6×10^{-3}	3.1×10^{-3}	1.6×10^{-2}	4.8×10^{-3}	2.8×10^{-2}	2.1×10^{-3}	0.079	4.5×10^{-3}	1.5×10^{-2}	1.9×10^{-2}
Y2w	4.9×10^{-3}	2.8×10^{-3}	1.8×10^{-3}	9.6×10^{-3}	2.5×10^{-3}	1.6×10^{-2}	1.2×10^{-3}	0.063	2.7×10^{-3}	7.7×10^{-3}	1.0×10^{-2}
Y3w	1.7×10^{-3}	5.8×10^{-4}	4.7×10^{-4}	2.7×10^{-3}	4.9×10^{-4}	5.4×10^{-3}	2.6×10^{-4}	0.043	7.2×10^{-4}	1.5×10^{-3}	2.2×10^{-3}
Y4w	3.3×10^{-4}	8.1×10^{-5}	8.1×10^{-5}	4.9×10^{-4}	6.8×10^{-5}	3.4×10^{-3}	5.8×10^{-5}	0.022	1.0×10^{-4}	2.2×10^{-4}	3.2×10^{-4}
Y5w*	1.2×10^{-4}	6.4×10^{-5}	1.4×10^{-5}	2.0×10^{-4}	5.6×10^{-6}	2.4×10^{-3}	4.2×10^{-6}	0.014	2.4×10^{-5}	1.1×10^{-5}	3.5×10^{-5}
Y1h	1.4×10^{-2}	1.7×10^{-2}	6.7×10^{-3}	3.7×10^{-2}	1.6×10^{-2}	7.3×10^{-2}	8.1×10^{-3}	0.12	8.4×10^{-3}	3.8×10^{-2}	4.7×10^{-2}
Y3h	4.5×10^{-3}	2.9×10^{-3}	1.9×10^{-3}	9.3×10^{-3}	3.2×10^{-3}	2.3×10^{-2}	1.9×10^{-3}	0.056	2.5×10^{-3}	6.8×10^{-3}	9.3×10^{-3}
Y5h*	7.4×10^{-5}	6.3×10^{-5}	8.7×10^{-6}	1.5×10^{-4}	1.0×10^{-5}	1.0×10^{-2}	3.2×10^{-5}	0.011	1.5×10^{-5}	7.5×10^{-6}	2.2×10^{-5}

*: These runs are not turbulent.

from the saturated state of these runs are also shown in Table 4. We see that at the same value of Am , the kinetic and magnetic energy density from the weak field simulations are smaller than those in our fiducial runs by a factor of 2-3. By inspection of the velocity field as well as the distribution of current density, we find that sustained turbulence is supported in run Y4w but not in run Y5w. Note that the time and volume averaged kinetic energy density from run Y4w is 4.9×10^{-4} , which is slightly below our limit of 10^{-3} , but the total stress $\alpha = 3.2 \times 10^{-4}$ is reasonably large and is unlikely to be caused by inertia waves in the simulation box. Further discussion will be given in the next subsection 3.2.4.

Together with the results from Section 3.2.1, we summarize the results from net toroidal flux simulations in Figure 10. We see that for both values of β_0 (100 and 400), we do not observe any sustained MRI turbulence for $Am < 3$. Although we have not explored weaker net toroidal flux, based on the trend we see from the Figure, even if MRI can be self-sustained at $Am \lesssim 1$ with weaker net toroidal flux, the resulting total stress α is unlikely to be above 10^{-4} . This is in stark contrast with the net vertical flux simulations, and indicates that pure toroidal field geometry is more stable in the AD dominated regime.

3.2.4. Criterion for Sustained Turbulence

A key objective of this paper is to study when MRI turbulence can be self-sustained in the presence of AD in the strong coupling limit. For the net vertical flux simulations, the criterion is relatively clear: turbulence can be sustained as long as the most MRI unstable mode fits into the simulation box. The situation is less clear for net toroidal flux simulations, and it remains to be seen whether the latter can be characterized as self-sustained turbulence.

We take run Y5 as an illustrative example in this subsection, but the analysis also applies to other marginal runs including Z6, Y5w, Y5h. In run Y5, after the initial turbulence has damped, the flow is largely laminar, except in a few very localized regions where some narrow but azimuthally elongated current structure is present and evolves very slowly with time. These features can

be better demonstrated by computing the vertically integrated Fourier power spectrum of magnetic and kinetic energies. Following the same procedure as described in Section 3.1.4 but integrating the full three-dimensional PSD over k_z , we show the contour plot of the kinetic energy PSD in the $k_x - k_y$ plane from our runs Y1, Y4 and Y5 in Figure 11. We see that in ideal MHD (Y1), the vertically integrated PSD has elliptic contours elongated and tilted toward the k_x axis. The contours are distorted and more elongated when AD is added (Y4). However, in run Y5, we see that the overall shape of the PSD contours are extremely elongated in the k_x direction. The original elliptic contours are almost destroyed, with irregular fragments distributed around the center. These irregular features in the vertically integrated PSD strongly indicate that the system is not in a turbulent state. We have also found that such irregular features are also present in runs Z6, Y5w and Y5h, but not present in runs Z5, Y4w and Y3h.

In sum, we conclude that non-zero kinetic energy density and total stress do not prove the existence of the MRI turbulence in shearing box simulations. Transition from self-sustained turbulence to non-turbulent state can be judged by looking at the vertically integrated PSD of kinetic and magnetic energies.

3.3. Simulations with both vertical and toroidal fluxes

Motivated by the linear stability analysis of the MRI with AD by Kunz & Balbus (2004) and Desch (2004), we present simulations that include both vertical and toroidal fluxes. These authors found that in the presence of both vertical and toroidal field, unstable modes exists for any values of Am , and the fastest growth rate is non-vanishing even as $Am \rightarrow 0^+$. When $Am \lesssim 1$, the wave number of the most unstable mode has a substantial non-zero radial component. In this subsection, we explore whether this behavior in the linear regime affects the non-linear evolution of the MRI with AD.

We use the vertical plasma β : $\beta_{z0} = 8\pi P_0 / B_z^2$ to specify the net vertical magnetic flux. The net toroidal flux is specified by its ratio to the net vertical field B_ϕ / B_z . We consider two sets of simulations, with $B_\phi / B_z = 4$ and $B_\phi / B_z = 1.25$ and labeled by letters “M” and “N”

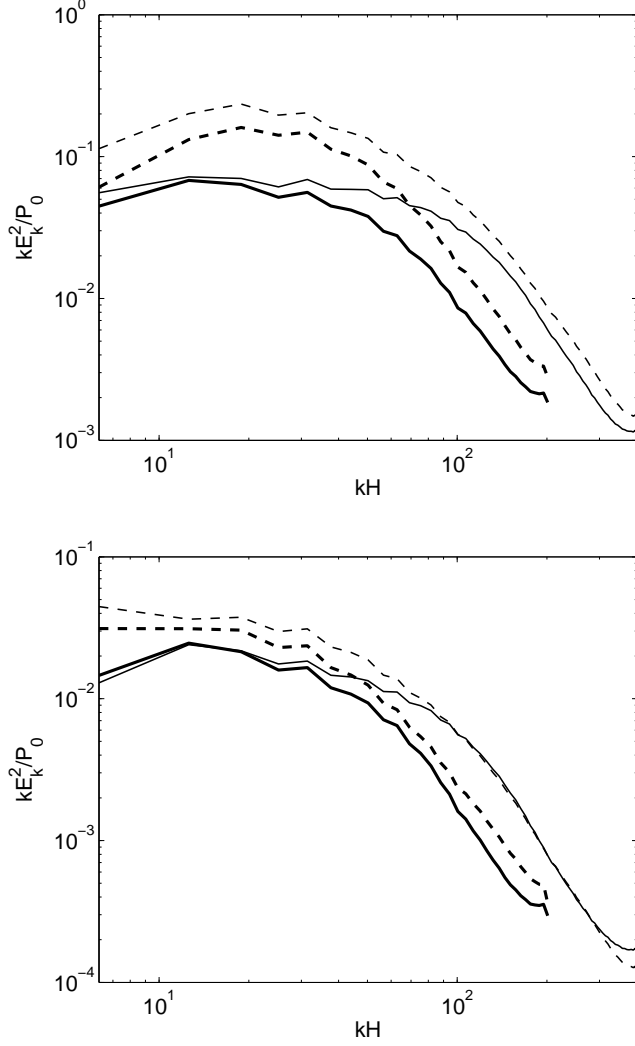


FIG. 9.— Similar to Figure 5, but for net toroidal flux simulations. Shown are the shell integrated power spectrum density of the kinetic (solid) and magnetic (dashed) energy densities. Upper panel: results from simulations with $Am = 1000$ (essentially ideal MHD). Our fiducial low-resolution results (run Y1) are shown in bold curves, while high-resolution results (run Y1h) are shown in thin lines. Lower panel: results from simulations with $Am = 10$, with low-resolution (run Y3) and high-resolution (Y3h) results shown in bold and thin lines. The uncertainty is about 10%.

respectively. Parameters of these runs are given in Table 5. Similar to the previous subsections, we scan the parameter Am from 1000 down to 0.1. We use the dispersion relation (31) - (35) in Kunz & Balbus (2004) to find the wavenumber of the most unstable mode. We find that for $Am \gtrsim 3$, the most unstable wavenumber is essentially purely vertical, while for $Am \lesssim 1$, the most unstable wavenumber is oblique with $k_z \sim -k_r$. Correspondingly, we choose the box size to be $H \times 4H \times H$ for runs with $Am \geq 3$ and $4H \times 4H \times H$ for $Am \leq 1$. For simulations with $Am \leq 1$, we expect the fastest growth of the MRI to occur in the diagonal direction of the $x-z$ plane.

By default, we fix $\beta_{z0} = 1600$ in both sets of simulations. However, as Am falls below 1, we find that the fastest growing mode will no longer fit into our simulation

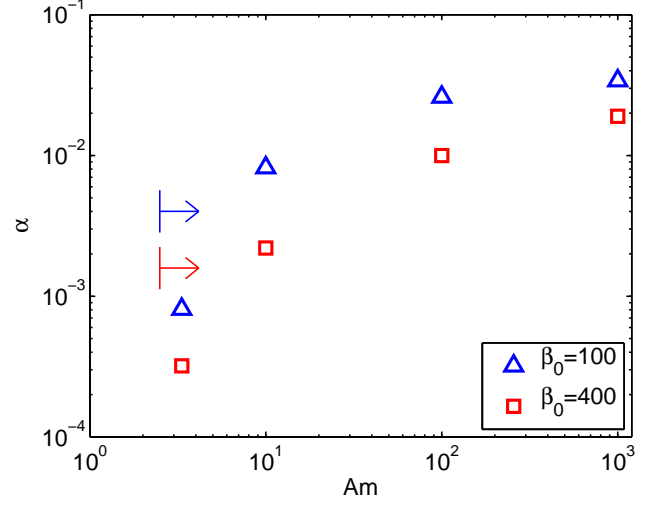


FIG. 10.— The time and volume averaged total stress α from our net toroidal flux simulations. Simulations with different net toroidal flux, characterized by the plasma β_0 , are labeled by different symbols and colors. The arrows for each β_0 (as represented in red and blue) indicate the range of Am where MRI turbulence can be sustained.

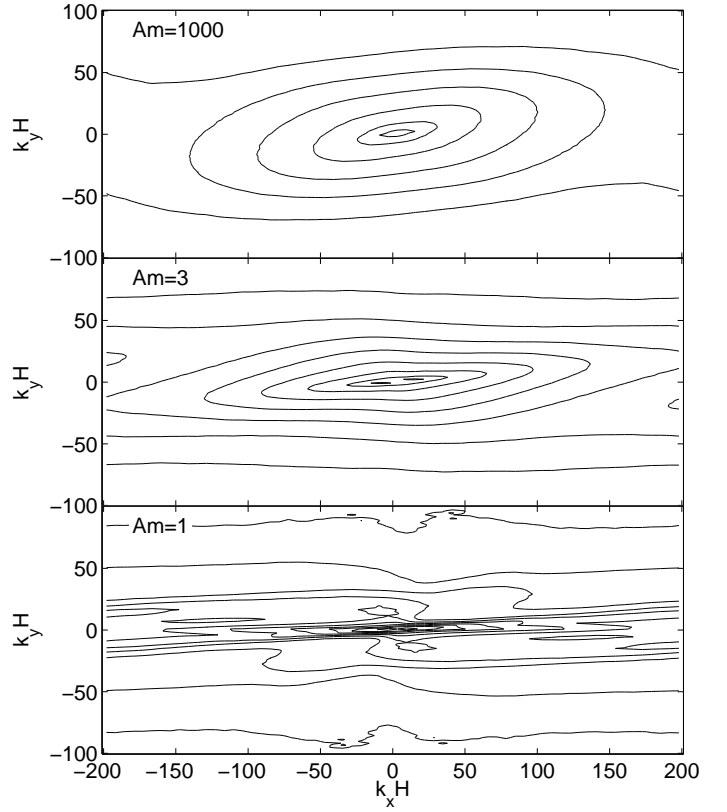


FIG. 11.— Contour plot of the vertically integrated power spectrum density of kinetic energy from our net toroidal flux simulation runs Y1 ($Am = 1000$), Y4 ($Am = 3$) and Y5 ($Am = 1$). Neighboring contours are separated by a factor of 10 in the power spectrum density.

TABLE 5
SIMULATIONS WITH BOTH NET VERTICAL AND TOROIDAL FLUXES.

Run	Am	Box size	β_{z0}^1	B_ϕ/B_z	Orbits
M1	1000	$H \times 4H \times H$	1600	4	48
M2	100	$H \times 4H \times H$	1600	4	48
M3	10	$H \times 4H \times H$	1600	4	36
M4	3.33	$H \times 4H \times H$	1600	4	36
M5	1	$4H \times 4H \times H$	1600	4	42
M6	0.33	$4H \times 4H \times H$	8000	4	96
M7	0.1	$4H \times 4H \times H$	30000	4	96
N1	1000	$H \times 4H \times H$	1600	1.25	48
N2	100	$H \times 4H \times H$	1600	1.25	48
N3	10	$H \times 4H \times H$	1600	1.25	48
N4	3.33	$H \times 4H \times H$	1600	1.25	48
N5	1	$4H \times 4H \times H$	1600	1.25	46
N6	0.33	$4H \times 4H \times H$	1600	1.25	96
N7	0.1	$4H \times 4H \times H$	8000	1.25	96

The grid resolution is fixed at 64 cells per H . All simulations are initiated from seed perturbations, and generate sustained turbulence.

¹: plasma β from the vertical magnetic field.

box. Based on the results from Section 3.1, MRI turbulence would not be sustained in this case. Therefore, we increase β_{z0} to the value such that the most unstable mode just fit into the box. In the case of $B_\phi/B_z = 4$, β_{z0} is increased to 8000 and 3×10^4 for $Am = 0.33$ and $Am = 0.1$ respectively. For $B_\phi/B_z = 1.25$, we increase β_{z0} to 8000 at $Am = 0.1$. Consequently, for all simulations in this subsection, MRI grows from the initial seed perturbations, and generates sustained turbulence after saturation. Below we discuss the properties of the MRI turbulence in the two sets of simulations.

The first group of simulations (with $B_\phi/B_z = 4$) are run for at least 36 orbits. The initial growth of the MRI from runs M5 ($Am = 1$), M6 ($Am = 0.33$) and M7 ($Am = 0.1$) are slower than the ideal MHD limit due to strong effect of AD: the fastest growth rates σ_m predicted from the linear dispersion relation for these simulation runs are $0.189\Omega^{-1}$, $0.149\Omega^{-1}$ and $0.136\Omega^{-1}$ respectively. This is to be compared with the case with pure vertical field with the same Am , where the corresponding σ_m is $0.428\Omega^{-1}$, $0.218\Omega^{-1}$ and $0.074\Omega^{-1}$ respectively. The presence of both vertical and toroidal field gives a smaller growth rate at relatively large Am , but σ_m decreases much slower with decreasing Am than the pure vertical field case. At $Am \lesssim 0.1$, a field configuration with both net vertical and toroidal fluxes becomes more favorable than the pure net vertical field geometry by having substantially larger σ_m .

In the second group of runs, we choose $B_\phi/B_z = 1.25$, which generates the fastest grow rate at $Am \leq 1$ compared with any other values. The fastest growth rates σ_m for runs N5 ($Am = 1$), N6 ($Am = 0.33$) and N7 ($Am = 0.1$) are $0.371\Omega^{-1}$, $0.253\Omega^{-1}$ and $0.206\Omega^{-1}$ respectively, which are nearly two times larger than those for $B_\phi/B_z = 4$.

Our simulations with $Am \leq 1$ (M5-M7, N5-N7) are particularly interesting because the fastest growing mode has a non-zero radial wave number $|k_r|$ comparable to $|k_z|$. During the linear growth stage, we observe axisymmetric structures in the $x - z$ plane similar to channel

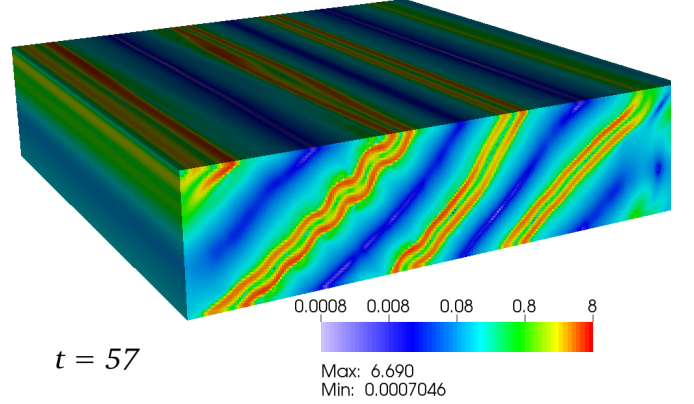


FIG. 12.— The distribution of current density in run M5 with $Am = 1$, $B_\phi/B_z = 4$ at the break down of the “channel flow” before saturating into turbulence (at time $t = 57\Omega^{-1}$).

modes, but tilted toward the diagonal direction. These structures grow to a large amplitude, and finally break down into turbulence. As an example, we show in Figure 12 the distribution of current density right before the break down of the channel flow for run M5. In the turbulent state, one can still observe the emergence of structures elongated in the diagonal direction in the $x - z$ plane from time to time, which then fragment and inject kinetic energy into the system. For the simulations with $Am \leq 0.33$, these events lead to sporadic increase of kinetic energy and Reynolds stress on time scales of 10 – 20 orbits. Due to such long time variability, we run these models for longer (to 96 orbits) and take the time average from about 56 orbits ($350\Omega^{-1}$) onward.

The time and volume averaged properties of the MRI turbulence in all simulations with both net vertical and toroidal fluxes are listed in Table 6. In Figure 13 we plot the total turbulent stress α as a function of Am from the two groups of simulations. We see that at $Am \gtrsim 1$, where all simulations have the same net vertical flux $\beta_{z0} = 1600$, runs with $B_\phi/B_z = 4$ generate slightly stronger MRI turbulence than simulations with $B_\phi/B_z = 1.25$. This trend can be extrapolated down to zero net toroidal flux, as one can compare with results in runs Z3w and Z5w in Table 2. The dependence of turbulent strength on the toroidal flux is relatively weak, and when the net vertical flux is doubled, as in runs Z1 to Z5, the strength of the turbulence becomes stronger than our corresponding runs M1 to M5.

For simulations with $Am < 1$, we find that the turbulent stress α exceeds the maximum possible α attainable by the pure net vertical flux simulations. At $Am = 0.1$, the maximum value of α is 6.1×10^{-4} , as compared to about 9.7×10^{-5} from the pure net vertical flux case. This

TABLE 6
TIME AND VOLUME AVERAGED QUANTITIES IN SIMULATIONS WITH BOTH NET VERTICAL AND NET TOROIDAL FLUXES.

Run	$E_{k,x}$	$E_{k,y}$	$E_{k,z}$	E_k	$E_{M,x}$	$E_{M,y}$	$E_{M,z}$	$\langle \delta \rho \rangle / \rho_0$	α_{Re}	α_{Max}	α
M1	5.6×10^{-2}	5.8×10^{-2}	1.9×10^{-2}	0.13	6.7×10^{-2}	0.30	2.8×10^{-2}	0.26	3.4×10^{-2}	0.17	0.21
M2	4.2×10^{-2}	3.4×10^{-2}	1.2×10^{-2}	8.8×10^{-2}	4.3×10^{-2}	0.17	2.0×10^{-2}	0.16	2.4×10^{-2}	0.10	0.13
M3	1.6×10^{-2}	9.2×10^{-3}	5.7×10^{-3}	3.1×10^{-2}	1.1×10^{-2}	5.3×10^{-2}	6.3×10^{-3}	0.087	9.1×10^{-3}	2.8×10^{-2}	3.7×10^{-2}
M4	9.5×10^{-3}	4.7×10^{-3}	3.7×10^{-3}	1.8×10^{-2}	3.9×10^{-3}	2.2×10^{-2}	3.3×10^{-3}	0.075	4.7×10^{-3}	8.7×10^{-3}	1.3×10^{-2}
M5	3.9×10^{-3}	2.8×10^{-3}	1.4×10^{-3}	8.1×10^{-3}	1.3×10^{-3}	1.3×10^{-2}	1.7×10^{-3}	0.066	1.7×10^{-3}	2.8×10^{-3}	4.5×10^{-3}
M6	1.7×10^{-3}	2.1×10^{-3}	2.2×10^{-4}	4.0×10^{-3}	1.3×10^{-4}	2.6×10^{-3}	3.1×10^{-4}	0.058	5.6×10^{-4}	4.0×10^{-4}	9.6×10^{-4}
M7	1.4×10^{-3}	4.0×10^{-4}	6.5×10^{-5}	1.9×10^{-3}	3.0×10^{-5}	7.6×10^{-4}	7.3×10^{-5}	0.050	4.8×10^{-4}	1.3×10^{-4}	6.1×10^{-4}
N1	3.8×10^{-2}	3.9×10^{-2}	1.4×10^{-2}	9.1×10^{-2}	4.2×10^{-2}	0.20	1.8×10^{-2}	0.20	2.2×10^{-2}	0.12	0.14
N2	2.8×10^{-2}	2.2×10^{-2}	9.4×10^{-3}	5.9×10^{-2}	2.7×10^{-2}	0.11	1.3×10^{-2}	0.13	1.6×10^{-2}	6.8×10^{-2}	8.3×10^{-2}
N3	1.4×10^{-2}	6.7×10^{-3}	4.5×10^{-3}	2.5×10^{-2}	7.4×10^{-3}	3.6×10^{-2}	4.4×10^{-3}	0.080	6.9×10^{-3}	2.0×10^{-2}	2.7×10^{-2}
N4	6.3×10^{-3}	3.4×10^{-3}	2.9×10^{-3}	1.3×10^{-2}	1.7×10^{-3}	9.2×10^{-3}	2.1×10^{-3}	0.068	2.6×10^{-3}	4.6×10^{-3}	7.3×10^{-3}
N5	3.2×10^{-3}	1.8×10^{-3}	1.3×10^{-3}	6.3×10^{-3}	5.2×10^{-4}	4.7×10^{-3}	1.3×10^{-3}	0.065	1.2×10^{-3}	1.8×10^{-3}	3.0×10^{-3}
N6	1.2×10^{-3}	1.1×10^{-3}	9.0×10^{-4}	3.2×10^{-3}	1.2×10^{-4}	1.8×10^{-3}	8.7×10^{-4}	0.057	3.8×10^{-4}	4.8×10^{-4}	8.6×10^{-4}
N7	9.9×10^{-4}	2.4×10^{-4}	1.1×10^{-4}	1.3×10^{-3}	2.9×10^{-5}	5.7×10^{-4}	1.8×10^{-4}	0.042	3.0×10^{-4}	1.6×10^{-4}	4.7×10^{-4}

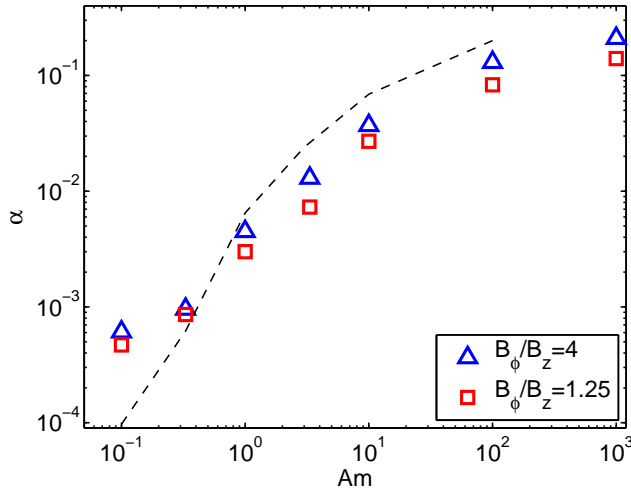


FIG. 13.— The time and volume averaged total stress α from our simulations with both net vertical and net toroidal flux. Shown are results from two groups of simulations with different ratio B_ϕ/B_z , are labeled by different symbols and colors. Dashed line represents the maximum value of α obtained from pure net vertical flux simulations (Figure 4).

is consistent with the linear dispersion properties discussed before: the presence of both vertical and toroidal field raises the maximum growth rate in the $Am < 1$ regime. While the values of α given by the $B_\phi/B_z = 4$ group are still larger than those in the $B_\phi/B_z = 1.25$ group, the latter group produces larger Maxwell stress. We note that for $Am \leq 1$, we have chosen the largest possible net flux such that the vertical extent of the simulation box can fit only one most unstable mode. According to the discussion in Section 3.1.2, the strength of the MRI turbulence from these simulations represents the highest possible level at the given value of Am and the given magnetic field geometry for our box size, and may also approach the highest level in real disks.

4. MRI WITH AMBIPOLAR DIFFUSION: DIAGNOSTICS

In this section, we combine the results from all our simulations and further discuss the criteria for whether the MRI can be self-sustained with AD in a more general

context.

The MRI acts as a dynamo which amplifies initially weak fields. Although the saturation mechanism of the MRI is not well understood (but see Pessah & Goodman (2009); Pessah (2010)), the magnetic field energy at the saturated state scales with the net magnetic flux and is generally below equipartition with thermal energy (Hawley et al. (1995); Sano et al. (1998) as well as this paper). Given the field geometry, there should exist a one-to-one correspondence between the initial field strength characterized by β_0 and the final field strength characterized by $\langle \beta \rangle$ (the space and time averaged gas to magnetic pressure at the saturated state), with $\langle \beta \rangle < \beta_0$ for weak field due to the MRI dynamo, and gradually transiting to $\langle \beta \rangle \approx \beta_0$ where the background field is too strong field to be destabilized.

The quantity $\langle \beta \rangle$ is also very useful for studying non-ideal MHD effects because the value it controls the relative importance of various non-ideal MHD effects (Ohmic, Hall and AD, e.g., see Wardle (2007); Bai (2011)). Henceforth, we shall consider $\langle \beta \rangle$ as a main diagnostic quantity on the MRI turbulence.

In Figure 14 we show the scattered plot of α and $\langle \beta \rangle$ from all our simulations with sustained turbulence with different field geometries. We see that regardless of the initial field geometry and the value of Am , there is a remarkably tight correlation between the two quantities at the saturated state of the MRI turbulence. The correlation can be represented by

$$\langle \beta \rangle \approx \frac{1}{2\alpha}. \quad (23)$$

This result is consistent with findings by (Hawley et al. 1995) in ideal MHD simulations, and extends it to the non-ideal MHD regime. Analytical study of the saturation of the MRI with Ohmic resistivity by parasitic modes also predicts similar relations (Pessah 2010). More explicitly, this relation translates to

$$\overline{B^2} \approx 4\overline{B_r B_\phi} (1 + R), \quad (24)$$

where R is the ratio of Reynolds to Maxwell stress (typically $\approx 1/3$ in the ideal MHD case). This relation implies

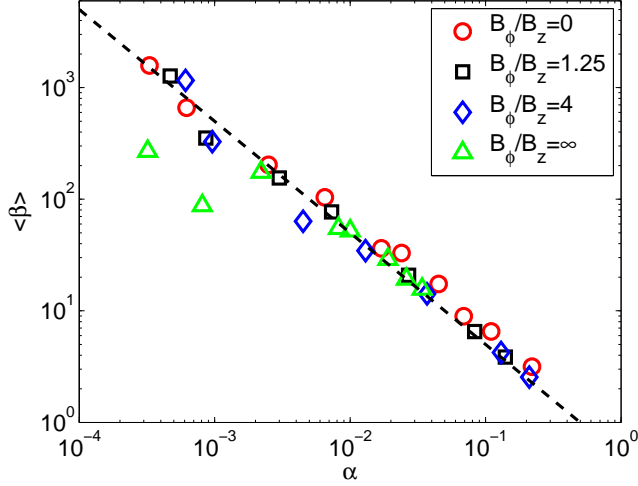


FIG. 14.— Scattered plot of the total turbulent stress α and the plasma β at the saturated state of the MRI turbulence from all our simulations. Simulations with different field geometries are marked by different symbols and colors as indicated in the legend, where $B_\phi/B_z = 0$ and $B_\phi/B_z = \infty$ correspond to pure net vertical and pure net toroidal flux simulations respectively. Dashed line shows the fitting curve $\langle\beta\rangle = 1/2\alpha$.

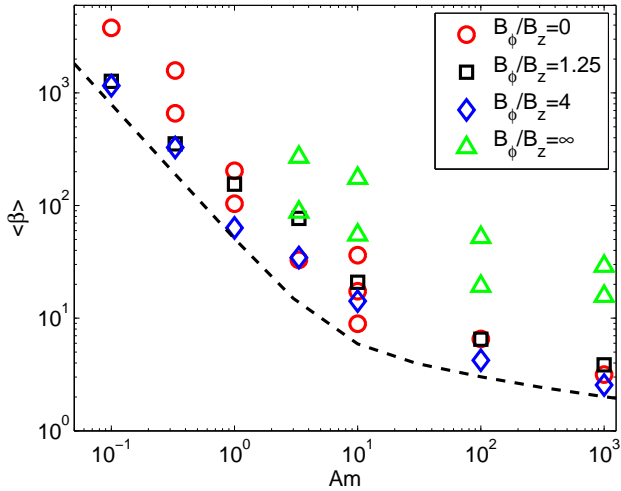


FIG. 15.— Scattered plot of AD coefficient Am and the plasma β at the saturated state of the MRI turbulence from all our simulations. Simulations with different field geometries are marked by different symbols and colors as indicated in the legend. The dashed curve shows the fitting formula (25) as a lower bound of $\langle\beta\rangle \geq \beta_{\min}(Am)$.

that the Maxwell stress is approximately a fixed fraction of the total magnetic energy, a reasonable result if the magnetic field is dominated by turbulent fluctuations. Only two points appear to deviate from this correlation, which correspond to net toroidal flux simulations with $Am = 3$. We see from Table 4 that in these two simulations, the magnetic energy is dominated by the background toroidal field (i.e., in the transition where MRI is marginally sustained), therefore producing smaller $\langle\beta\rangle$ than predicted.

Next, we consider the relation between $\langle\beta\rangle$ and Am . In Figure 15 we show scattered plot of Am and $\langle\beta\rangle$. We

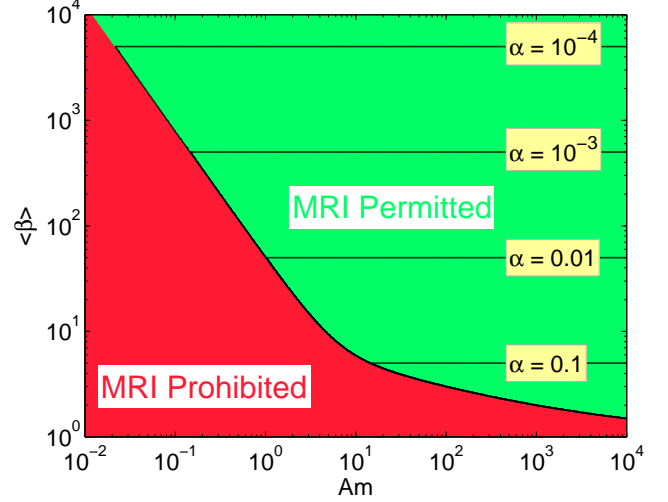


FIG. 16.— Diagnostics of the MRI in the AD regime. At a given Am , MRI is permitted when $\langle\beta\rangle \geq \beta_{\min}(Am)$ (see equation (25)), and in the MRI permitted region, the stress α can be inferred given the field strength at the saturated state characterized by $\langle\beta\rangle$.

see that $\langle\beta\rangle$ does not strongly correlate with Am , but also depends on the field geometry and the initial field strength. However, combining the simulation from all field geometries allow us to identify the lower bound of $\langle\beta\rangle$ at a given Am , denoted by β_{\min} , below which the field is too strong for to be destabilized based on our discussions before. For $Am \leq 1$, we have performed simulations with the smallest possible β_0 such that the most unstable mode marginally fit into the disk height H , and the value of β_{\min} identified in this regime is robust. For $Am > 1$, the exploration on β_0 may not be as complete especially in the simulations with both net vertical and toroidal fluxes and the actual β_{\min} may be somewhat smaller than obtained here. Nevertheless, this regime is closer to ideal MHD and is less concerning. By combining all the available simulations, we obtain a fitting formula for β_{\min} given by

$$\beta_{\min}(Am) = \left[\left(\frac{50}{Am^{1.2}} \right)^2 + \left(\frac{8}{Am^{0.3}} + 1 \right)^2 \right]^{1/2}, \quad (25)$$

and is indicated in Figure 15. It asymptotes to 1 at $Am \rightarrow \infty$ as one expects, while approaches $50/Am^{1.2}$ for $Am \lesssim 1$.

The constraint on β_{\min} at a given Am allows us to identify the regions in the Am - $\langle\beta\rangle$ plane at which MRI can or can not operate. In the mean time the correlation between α and $\langle\beta\rangle$ provide the corresponding stress when MRI is permitted. Combining them together, the main results from the whole paper are best summarized in Figure 16. MRI permitted regions are in the upper right with the boundary given by equation (25). It provides useful diagnostics on the properties of the MRI in the AD regime in a concise fashion.

First, at a given Am , the ultimate strength of the MRI turbulence (e.g., α and $\langle\beta\rangle$) depends on the field geometry (including the net flux), but there exists a maximum α (or minimum $\langle\beta\rangle$) at the most favorable field geometry (usually contains both net vertical and toroidal fluxes). One way to think about it is to starts with a weak reg-

ular field as we perform our simulations. As the system evolves and as the MRI amplifies the field, the corresponding position of the system in the diagram moves downward and until it stops at some $\langle\beta\rangle \gtrsim \beta_{\min}$.

Second, MRI can be self-sustained for any value of Am even for $Am \ll 1$. Although we have explored the Am parameter down to $Am = 0.1$, we believe that it can be extended to further smaller Am because of the following reasons. Linear analysis by Kunz & Balbus (2004) and Desch (2004) shows in the presence of both vertical and toroidal field, MRI can grow at appreciable rate (approximately $0.13\Omega^{-1}$ when $B_\phi/B_z = 4$) even in the limit of $Am \rightarrow 0^+$ provided that the field is sufficiently weak. This means that MRI turbulence can always be self-sustained. Meanwhile, we find that the linear dispersion relation has already approached the small Am asymptote for $Am \lesssim 0.3$. Therefore, we expect the trend in Figure 15 on β_{\min} to hold to further smaller Am values.

Third, the boundary between the MRI permitted and prohibited regions is only suggestive but it does not necessarily imply sharp transitions. Our simulations are restricted by the limited box height (H) since they are unstratified. In reality, as one increases the field strength, the transition from sustained MRI turbulence to its suppression involves the effect of vertical stratification of gas density in the disks, and may be a smooth process. Before justified by stratified simulations, which is left for our future work, this result should be taken with some caution. In particular, when vertical stratification is included, linear analysis by Gammie & Balbus (1994) and Salmeron & Wardle (2005) for ideal and non-ideal MHD have suggested the existence of global modes in the disk even in low β_0 and small Elsasser number. On the other hand, in the case of Ohmic resistivity, the criterion that Ohmic Elsasser number equals one being the boundary between MRI permitted and suppressed regions identified in unstratified simulations (Sano et al. 1998; Fleming et al. 2000; Sano & Stone 2002b) do agree with results from stratified simulations (Fleming & Stone 2003; Turner et al. 2007; Ilgner & Nelson 2008).

5. SUMMARY AND DISCUSSION

Weakly ionized plasma is subject to a number of non-ideal MHD effects due to the collisional coupling between the ionized species and the neutrals. Among them, ambipolar diffusion (AD) results from the relative motion between the ions and the neutrals. It becomes most important when the gyro-frequencies of both the electrons and the ions in the magnetic field are larger than their collision frequencies with the neutrals, so all ionized species are effectively coupled to the magnetic field. Consequently, AD usually dominates other non-ideal MHD effects (Ohmic resistivity and Hall effect) in regions with low density and high magnetic field. When the ion inertia is negligible and when the electron recombination time is much less than the dynamical time, AD is in the “strong coupling” limit, and can be studied by single-fluid models. In this limit, the effect of AD is fully characterized by the parameter Am , the number of times a neutral molecule/atom collide with the ions in a dynamical time, and is the equivalence of the Elsasser number

for Ohmic resistivity. The effect of AD becomes dynamically important when Am approaches order unity.

In weakly ionized disks such as the protoplanetary disks (PPDs), AD dominates other non-ideal MHD effects in the disk upper layer as well as the outer regions of the PPDs (Wardle 2007; Bai 2011). The magnetorotational instability (MRI), which is considered as the major mechanism for providing angular momentum transport via the MHD turbulence, is strongly affected by AD. In the linear regime, the growth of the MRI is reduced or suppressed in the presence of AD, depending on the value of Am and the magnetic field geometry (Blaes & Balbus 1994; Kunz & Balbus 2004; Desch 2004). Two-fluid simulations of the non-linear evolution of the MRI with AD by Hawley & Stone (1998) showed that significant turbulence and angular momentum transport occurs when $Am \gtrsim 100$. However, they ignored the processes of ionization and recombination, and the results are not directly applicable to the PPDs, where the strong coupling limit holds (Bai 2011).

We have implemented AD in the strong coupling limit in the Athena MHD code using a first-order accurate operator-split method. Its performance is verified by numerical tests on standing C-type shocks and the damping of MHD waves. We then perform local shearing box numerical simulations to study the effect of AD on the non-linear evolution of the MRI in the strong coupling limit. Our simulations are vertically unstratified with vertical box size equals the disk scale height H . The main purpose of this paper is to study how the properties of the MRI turbulence is affected by AD, especially the condition under which MRI turbulence can be self-sustained. We perform three groups of simulations with different magnetic field configurations, and the main results are summarized below.

1. Net vertical flux simulations. Unstable linear MRI modes always exist for any value of Am , with longer wavelength and smaller growth rate as Am gets smaller. MRI turbulence can be self-sustained as long as the wavelength of the most unstable mode λ_m is within H (so the vertical field has to be progressively weaker for $Am \rightarrow 0^+$). At fixed Am , the total turbulent stress α increases monotonically with net vertical flux, until reaches the maximum when $\lambda_m \approx H$. The maximum value of α rapidly decreases with Am when $Am < 10$, from about 0.4 at $Am \rightarrow \infty$ down to about 0.007 at $Am = 1$. It falls below 10^{-3} at $Am \approx 0.3$ and is around of 10^{-4} at $Am = 0.1$.
2. Net toroidal flux simulations. This field configuration is more stable. At fixed $Am \gtrsim 3$ and net flux, the turbulent stress α from net toroidal flux simulations is smaller than that from net vertical flux simulations by about an order of magnitude. We do not find any evidence that MRI turbulence can be self-sustained at the level of $\alpha \gtrsim 10^{-4}$ when $Am \lesssim 1$ for any net toroidal flux.
3. Simulations with both net vertical and net toroidal fluxes. When $Am \gtrsim 1$ and fixed net vertical flux, the strength of the MRI turbulence is similar to the pure net vertical flux case, but slowly increases

with the net toroidal flux. When $Am \lesssim 1$, the most unstable mode has non-zero radial wavenumber comparable to the vertical wavenumber, and the fastest growth rate asymptotes to some appreciable value even as $Am \rightarrow 0^+$. The maximum value of the turbulent stress α largely exceeds the pure net vertical flux case when $Am < 1$, with $\alpha \approx 6 \times 10^{-4}$ at $Am = 0.1$.

In addition, we find that similar to the effect of Ohmic dissipation, the ratio of the fluctuating part of the magnetic energy density to the kinetic energy density decreases as AD is stronger. Similarly, the ratio of Maxwell stress to Reynolds stress also drops at smaller Am . The power spectra density of the MRI turbulence in the AD dominated regime does not show any new features other than a rescaling from that in the ideal MHD case. We do not find any evidence that AD leads to the formation of sharp current structures in the MRI turbulence as proposed by Brandenburg & Zweibel (1994), but we confirm that AD tends to reduce the component of current perpendicular to the direction of magnetic field (Brandenburg et al. 1995), although to a lesser extent.

Combining the results from these three groups of simulations, we find a strong correlation between the turbulent stress α and the gas to magnetic pressure ratio β at the saturated state, given by $\langle \beta \rangle \approx 1/2\alpha$. The sustainability and saturation level of the MRI turbulence depends on the value of Am , the magnetic field geometry, and the magnetic field strength. It is best summarized in Figure 16. In short, at a given Am , there exists a maximum value of turbulent stress α achievable from the most favorable geometries (generally with both net vertical and toroidal fluxes). Correspondingly, at a given Am , there exists a maximum field strength above which MRI is suppressed, and the maximum field strength rapidly decreases with decreasing Am . For future reference, we quote the turbulent stress $\alpha = 7 \times 10^{-3}$ and 6×10^{-4} as the maximum value we have found in our simulations at $Am = 1$ and 0.1 respectively.

In principle, in the presence of both net vertical and net toroidal fluxes, MRI turbulence can be self-sustained at any values of Am , provided that the magnetic field is sufficiently small. Nevertheless, the resulting turbulent stress α would be much smaller than 6×10^{-4} when $Am < 0.1$, and would be inefficient in transporting angular momentum in most astrophysical disks. Moreover, we recall that AD dominates other non-ideal MHD ef-

fects (Ohmic resistivity and Hall effect) at relatively low density and relatively large magnetic field. When the magnetic field is too weak as required for the wavelength of the most unstable MRI mode to be within H , AD may no longer be the dominant non-ideal MHD effect, and our results are not directly applicable. Therefore, while generalization of our results to $Am < 0.1$ are possible, it may not be physically relevant.

We have shown that the effect of AD on the non-linear evolution of the MRI depends on the field geometry, which is arbitrarily assigned in our local shearing box simulations. In reality, the field geometry depends on the global evolution of the disk. Let us imagine one scenario and apply our local simulation results to a global picture. If the disk is initially threaded by a very weak vertical field (e.g., Armitage 1998), the initial growth of the MRI may be governed by the Ohmic resistivity and/or the Hall effect. AD takes over when substantial amplification of the field occurs and dominates the non-linear evolution of the MRI. The saturation of the MRI generates strong vertical and azimuthal fields, and redistributes the vertical and toroidal fluxes across the entire disk. No longer limited by the enforced net fluxes as in our local simulations, the saturation of the MRI could probably arrange the magnetic field to achieve the most favorable local field configurations such that the field is maximally amplified and $\langle \beta \rangle \approx \beta_{\min}$ is achieved. Therefore, given the value of Am in the disk, and provided that AD dominates other non-ideal MHD effects, we expect the field strength in the disk to be largely determined by the value of $\beta_{\min}(Am)$, via Equation (25), from which one can also obtain a rough estimate of $\alpha \approx 1/2\beta_{\min}$.

Our results are mostly relevant to the structure and evolution of the PPDs. Details about the application require considerations of the ionization and recombination processes in the disks with an appropriate chemistry model, which is beyond the scope of this paper. In our companion paper (Bai 2011), we will take into account all non-ideal MHD effects together and study their implications in the PPDs.

We thank Shane Davis for providing the code for analyzing the power spectrum and Jeremy Goodman for help discussions. This work is supported by NSF grant AST-0908269. X.-N.B. acknowledges support from NASA Earth and Space Science Fellowship.

REFERENCES

- Armitage, P. J. 1998, *ApJ*, 501, L189
 Bai, X. 2011, *ApJ*, in preparation
 Bai, X.-N. & Goodman, J. 2009, *ApJ*, 701, 737
 Balbus, S. A. 2003, *ARA&A*, 41, 555
 Balbus, S. A. & Hawley, J. F. 1991, *ApJ*, 376, 214
 —. 1992, *ApJ*, 400, 610
 Balbus, S. A. & Terquem, C. 2001, *ApJ*, 552, 235
 Balsara, D. S. 1996, *ApJ*, 465, 775
 Blaes, O. M. & Balbus, S. A. 1994, *ApJ*, 421, 163
 Bodo, G., Mignone, A., Cattaneo, F., Rossi, P., & Ferrari, A. 2008, *A&A*, 487, 1
 Brandenburg, A., Nordlund, A., Stein, R. F., & Torkelsson, U. 1995, *ApJ*, 446, 741
 Brandenburg, A. & Zweibel, E. G. 1994, *ApJ*, 427, L91
 Chiang, E., & Murray-Clay, R. 2007, *Nature Physics*, 3, 604
 Choi, E., Kim, J., & Wiita, P. J. 2009, *ApJS*, 181, 413
 Davis, S. W., Stone, J. M., & Pessah, M. E. 2010, *ApJ*, 713, 52
 Desch, S. J. 2004, *ApJ*, 608, 509
 Draine, B. T. 1980, *ApJ*, 241, 1021
 Falle, S. A. E. G. 2003, *MNRAS*, 344, 1210
 Fleming, T. & Stone, J. M. 2003, *ApJ*, 585, 908
 Fleming, T. P., Stone, J. M., & Hawley, J. F. 2000, *ApJ*, 530, 464
 Fromang, S. & Nelson, R. P. 2006, *A&A*, 457, 343
 Fromang, S. & Papaloizou, J. 2007, *A&A*, 476, 1113
 Gammie, C. F. 1996, *ApJ*, 457, 355
 Gammie, C. F. & Balbus, S. A. 1994, *MNRAS*, 270, 138
 Gardiner, T. A. & Stone, J. M. 2005, *Journal of Computational Physics*, 205, 509
 —. 2008, *Journal of Computational Physics*, 227, 4123
 Goldreich, P. & Lynden-Bell, D. 1965, *MNRAS*, 130, 125

- Goodman, J. & Xu, G. 1994, *ApJ*, 432, 213
- Hawley, J. F. 2000, *ApJ*, 528, 462
- . 2001, *ApJ*, 554, 534
- Hawley, J. F., Gammie, C. F., & Balbus, S. A. 1995, *ApJ*, 440, 742
- Hawley, J. F. & Stone, J. M. 1998, *ApJ*, 501, 758
- Ilgner, M. & Nelson, R. P. 2008, *A&A*, 483, 815
- Jin, L. 1996, *ApJ*, 457, 798
- Johnson, B. M., Guan, X., & Gammie, C. F. 2008, *ApJS*, 177, 373
- Kunz, M. W. & Balbus, S. A. 2004, *MNRAS*, 348, 355
- Li, P. S., McKee, C. F., & Klein, R. I. 2006, *ApJ*, 653, 1280
- Mac Low, M., Norman, M. L., Konigl, A., & Wardle, M. 1995, *ApJ*, 442, 726
- Masset, F. 2000, *A&AS*, 141, 165
- Miller, K. A. & Stone, J. M. 2000, *ApJ*, 534, 398
- Oishi, J. S. & Mac Low, M. 2009, *ApJ*, 704, 1239
- O’Sullivan, S. & Downes, T. P. 2006, *MNRAS*, 366, 1329
- . 2007, *MNRAS*, 376, 1648
- Papaloizou, J. C. B. & Terquem, C. 1997, *MNRAS*, 287, 771
- Pessah, M. E. 2010, *ApJ*, 716, 1012
- Pessah, M. E. & Chan, C. 2008, *ApJ*, 684, 498
- Pessah, M. E. & Goodman, J. 2009, *ApJ*, 698, L72
- Salmeron, R. & Wardle, M. 2005, *MNRAS*, 361, 45
- Sano, T., Inutsuka, S., & Miyama, S. M. 1998, *ApJ*, 506, L57
- Sano, T. & Stone, J. M. 2002a, *ApJ*, 570, 314
- . 2002b, *ApJ*, 577, 534
- Shakura, N. I. & Sunyaev, R. A. 1973, *A&A*, 24, 337
- Shen, Y., Stone, J. M., & Gardiner, T. A. 2006, *ApJ*, 653, 513
- Shu, F. 1991, *Physics of Astrophysics, Vol. II: Gas Dynamics*, ed. Shu, F. (University Science Books)
- Simon, J. B. & Hawley, J. F. 2009, *ApJ*, 707, 833
- Smith, M. D. & Mac Low, M. 1997, *A&A*, 326, 801
- Stone, J. M. 1997, *ApJ*, 487, 271
- Stone, J. M., Gammie, C. F., Balbus, S. A., & Hawley, J. F. 2000, *Protostars and Planets IV*, 589
- Stone, J. M. & Gardiner, T. A. 2010, *ApJS*, 189, 142
- Stone, J. M., Gardiner, T. A., Teuben, P., Hawley, J. F., & Simon, J. B. 2008, *ApJS*, 178, 137
- Stone, J. M., Hawley, J. F., Gammie, C. F., & Balbus, S. A. 1996, *ApJ*, 463, 656
- Tilley, D. A. & Balsara, D. S. 2008, *MNRAS*, 389, 1058
- Toth, G. 1994, *ApJ*, 425, 171
- Turner, N. J. & Sano, T. 2008, *ApJ*, 679, L131
- Turner, N. J., Sano, T., & Dziourkevitch, N. 2007, *ApJ*, 659, 729
- Wardle, M. 1999, *MNRAS*, 307, 849
- . 2007, *Ap&SS*, 311, 35
- Winters, W. F., Balbus, S. A., & Hawley, J. F. 2003, *MNRAS*, 340, 519